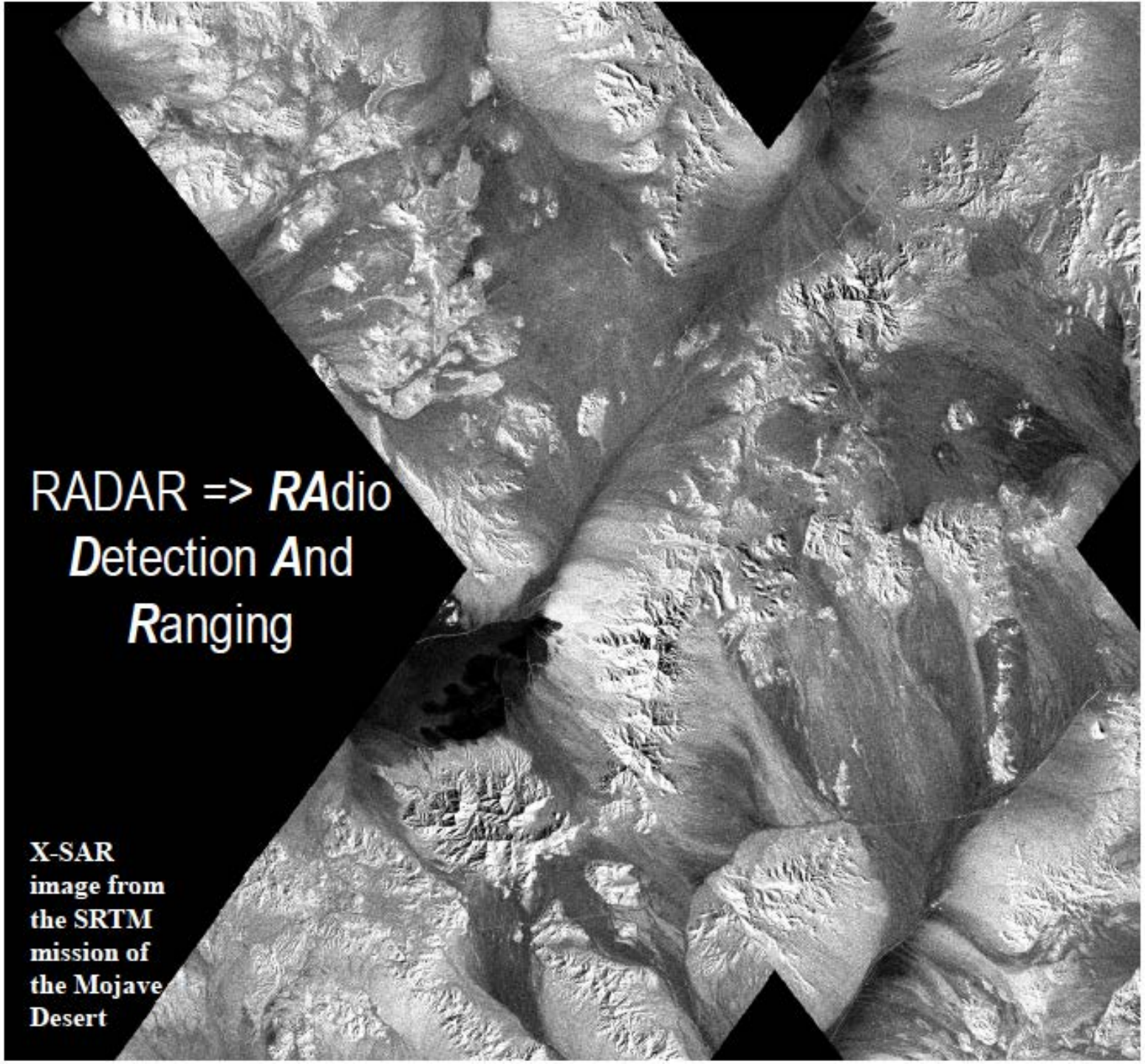
RADAR => RAdio
Detection And
Ranging
X-SAR
image from
the SRTM
mission of
the Mojave
Desert

Recall: Fresnel's equations…

give the reflection, transmission coefficients as functions of θ_1, θ_2, polarization

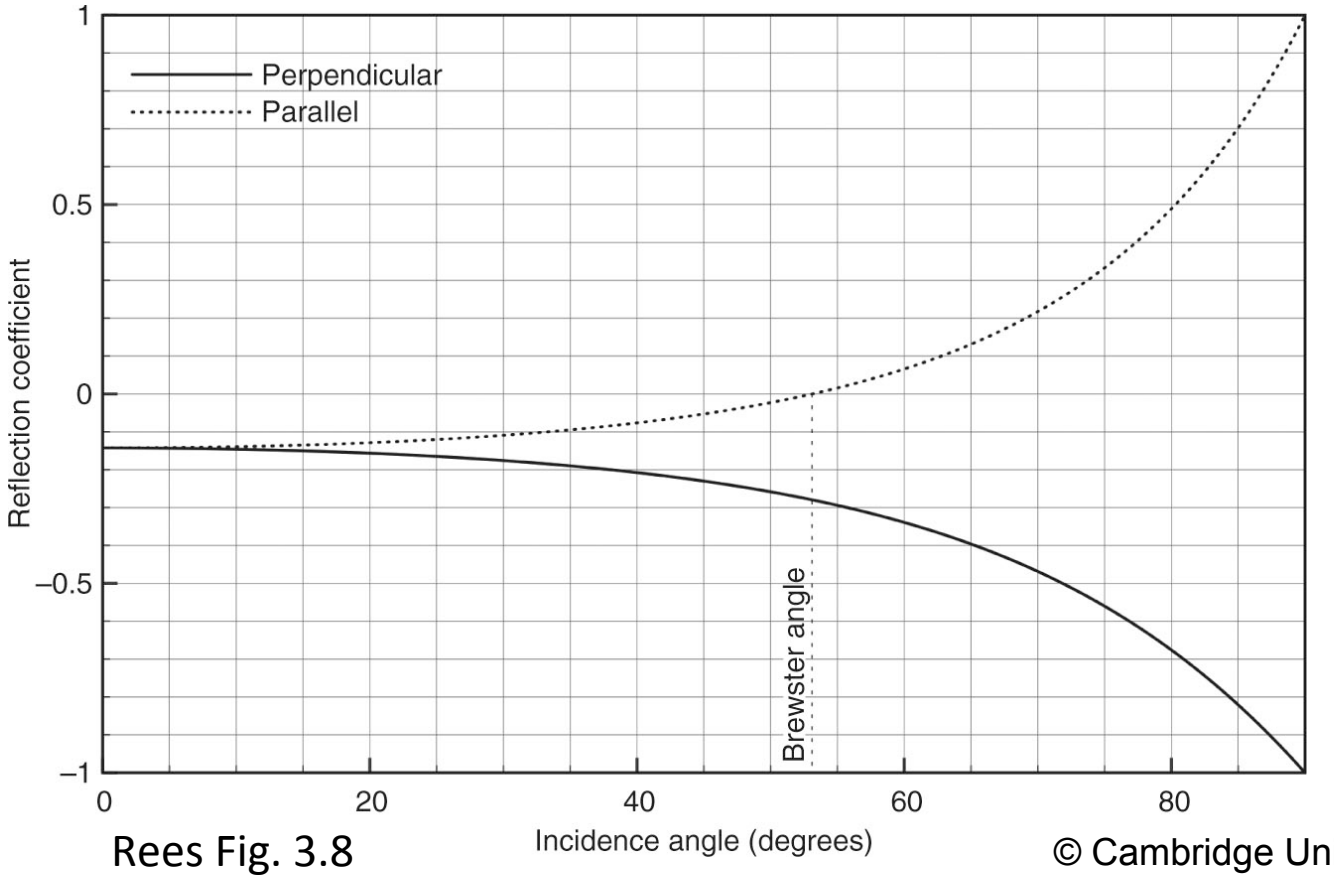

Rees Fig. 3.8

POLARIMETRIC SYNTHETIC APERTURE RADAR

WAVE POLARIZATIONS: EXAMPLES

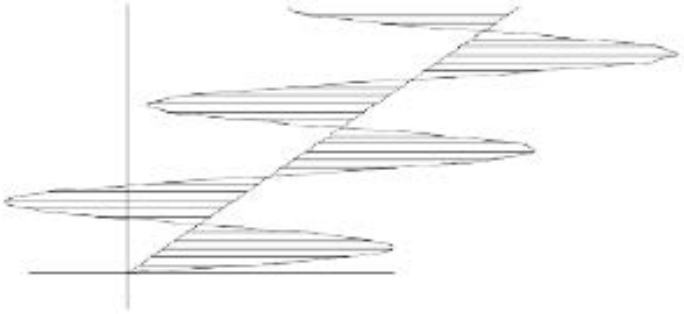

HORIZONTAL (LINEAR)

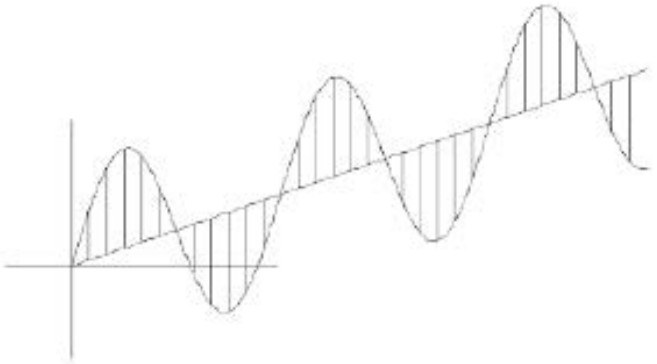

VERTICAL (LINEAR)

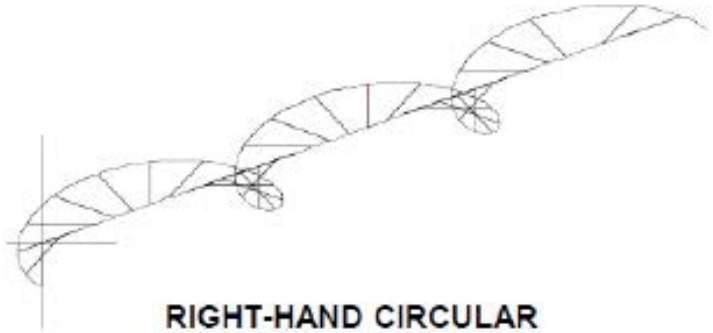

RIGHT-HAND CIRCULAR

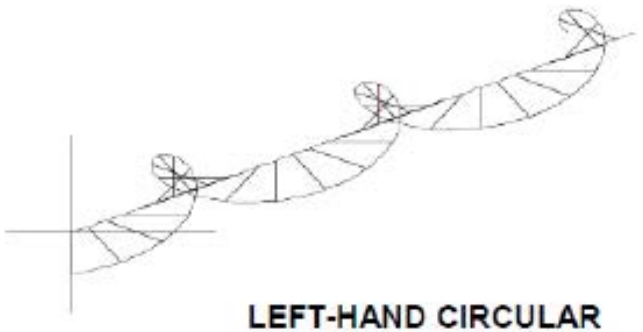

LEFT-HAND CIRCULAR

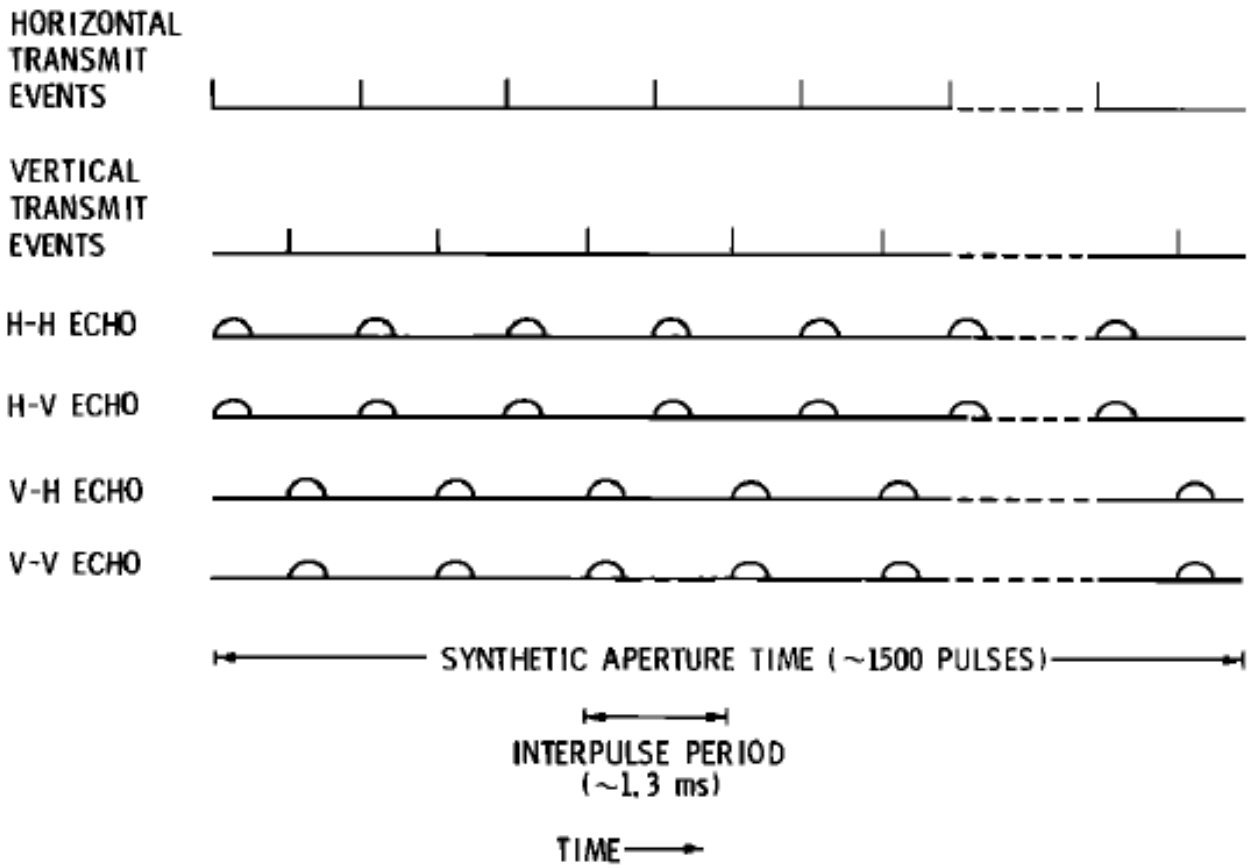

Fig. 4. Near simultaneity is achieved from overlapping sets of pulses. Each horizontally polarized transmit pulse and vertically polarized transmit pulse is offset in time from the other by one half the interpulse period, typically 0.5–1.0 ms. In the data processor we form a synthetic aperture by coherent integration of many pulses; however, pulses corresponding to each different polarization combination are isolated and integrated independently of the other pulses. The total coherent integration required to achieve 3-m single-look resolution consists of approximately 1500 pulses over a 2-s period; therefore the interspersed sets of pulses correspond to very nearly the same synthesized spatial array.

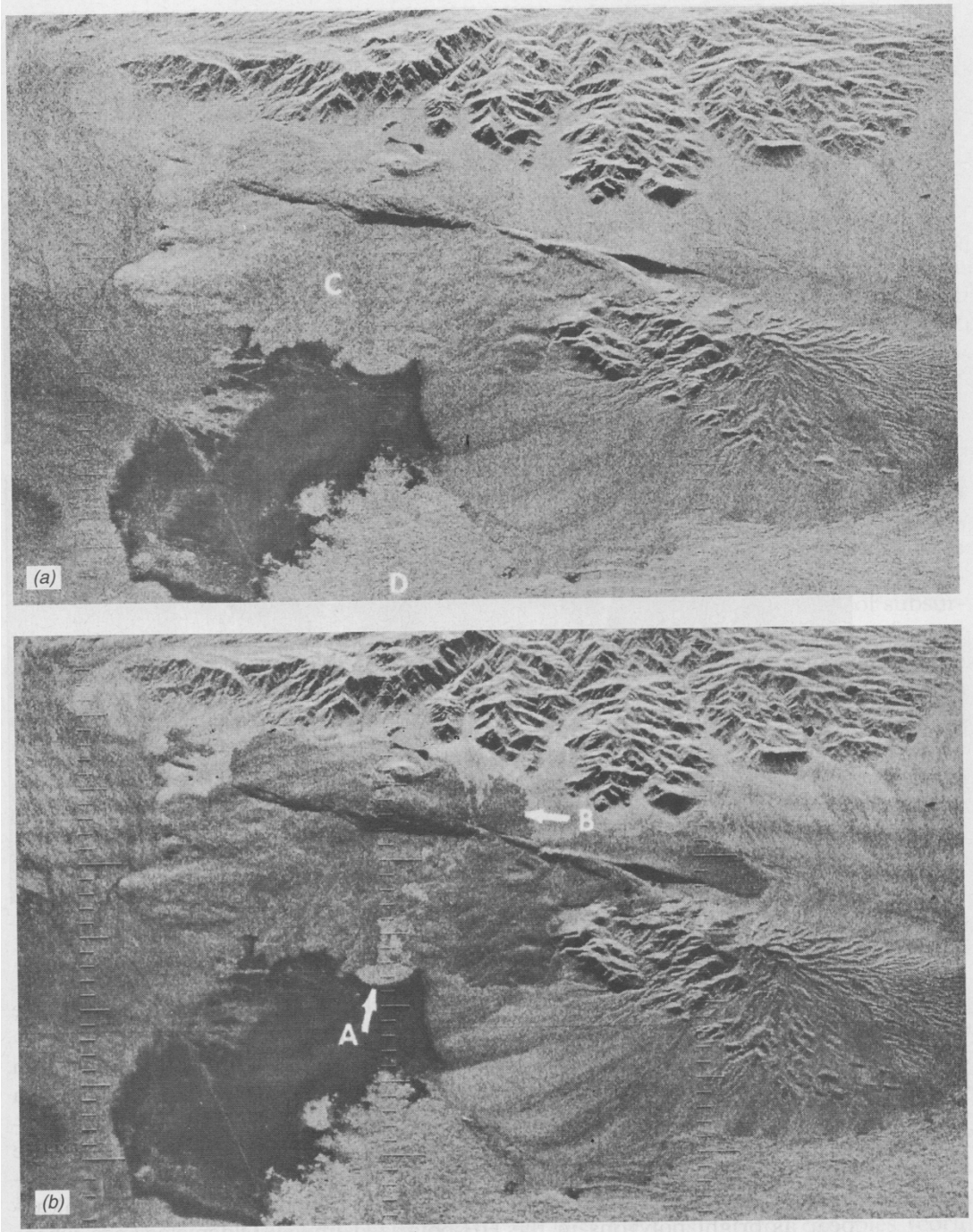

Figure 8.27 SLR images, Sunshine Crater Area, CA, K band, real aperture (scale 1:75,000): (*a*) HH polarization; (*b*) HV polarization. (Courtesy Westinghouse Electric Corp.)

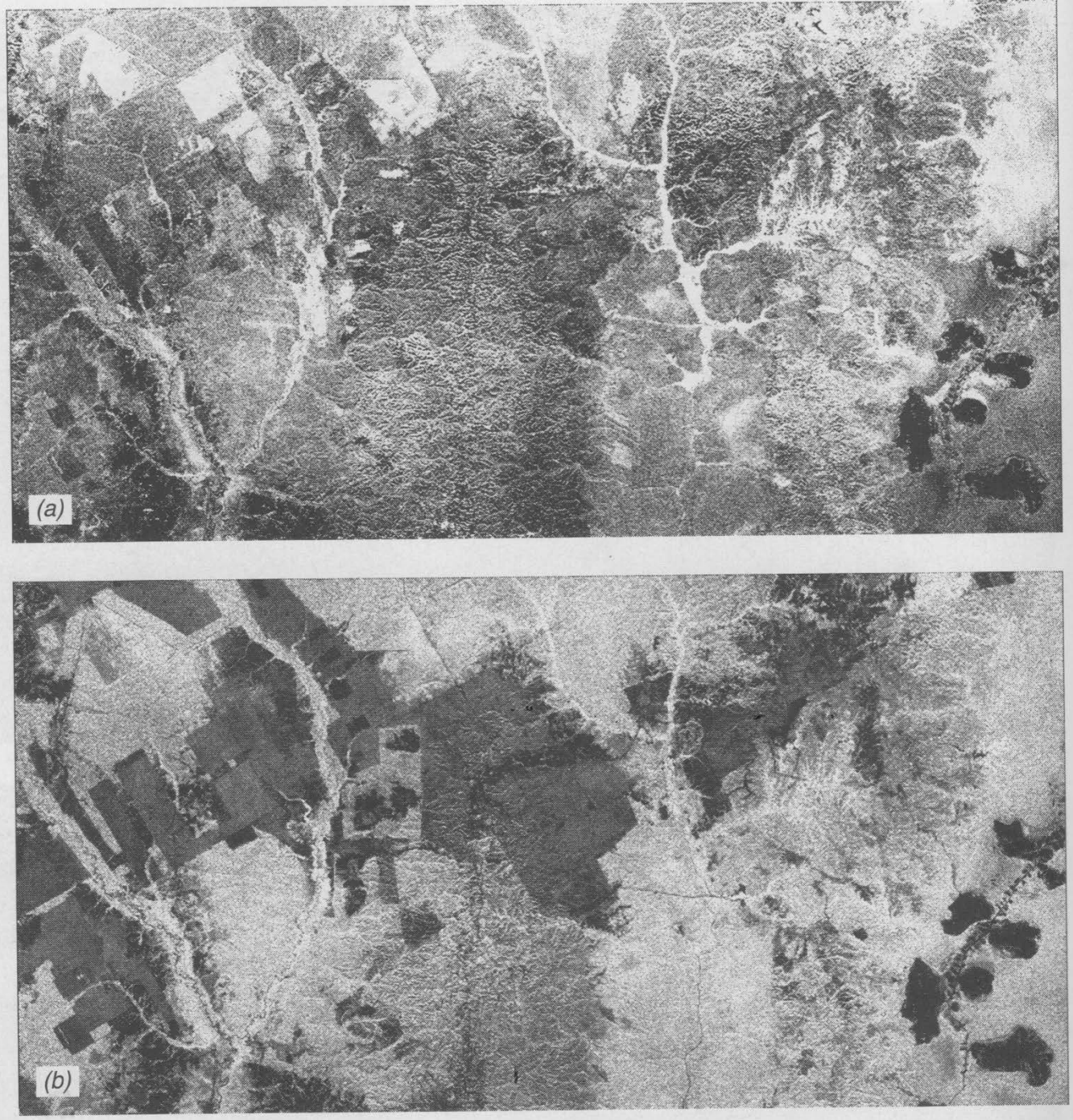

Figure 8.28 SIR-C radar images of Sumatra, Indonesia. (*a*) L-HH. (*b*) L-HV. (Courtesy NASA/JPL/Caltech.)

Brazil - Forest Inundation

SIR-C/X-SAR
MANAUS, BRAZIL SUPERSITE
INUNDATION MAP
APRIL 12, 1994

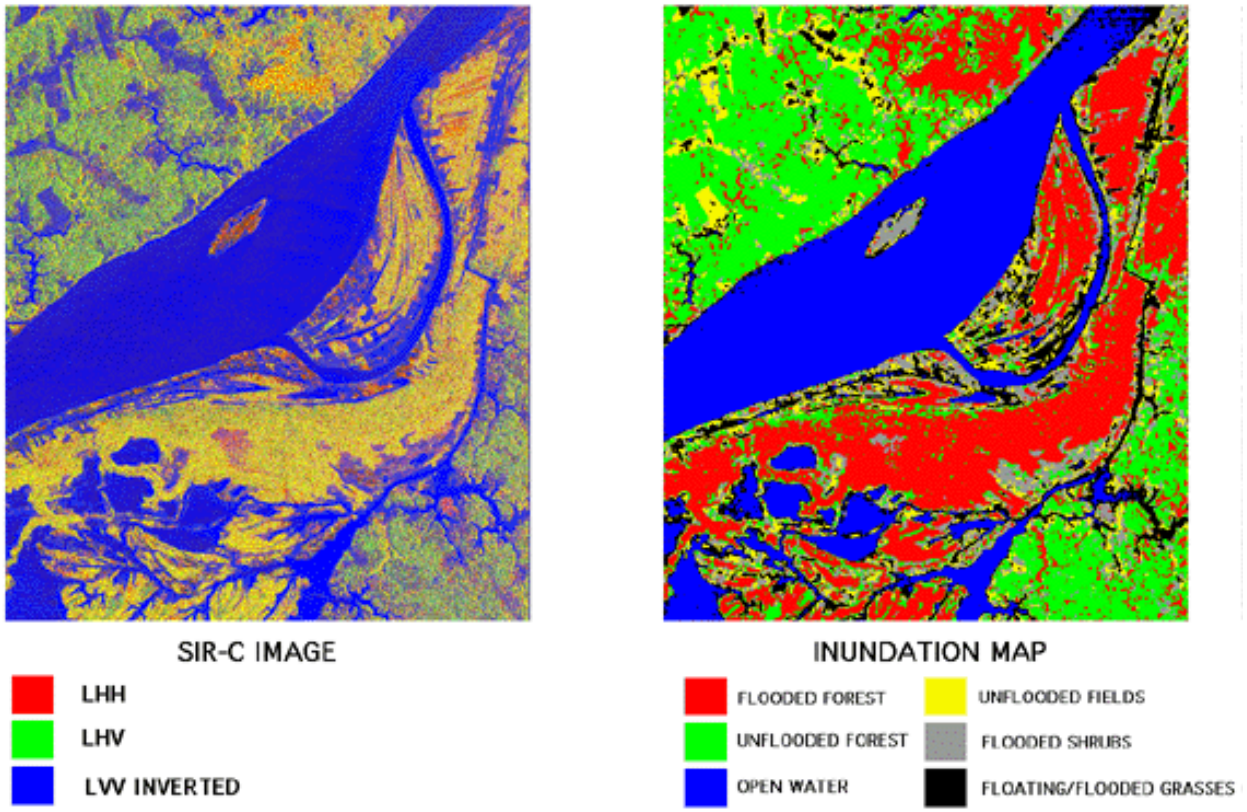

Mt. Rainier

R - Lhh, G - Lhv, B - Chv

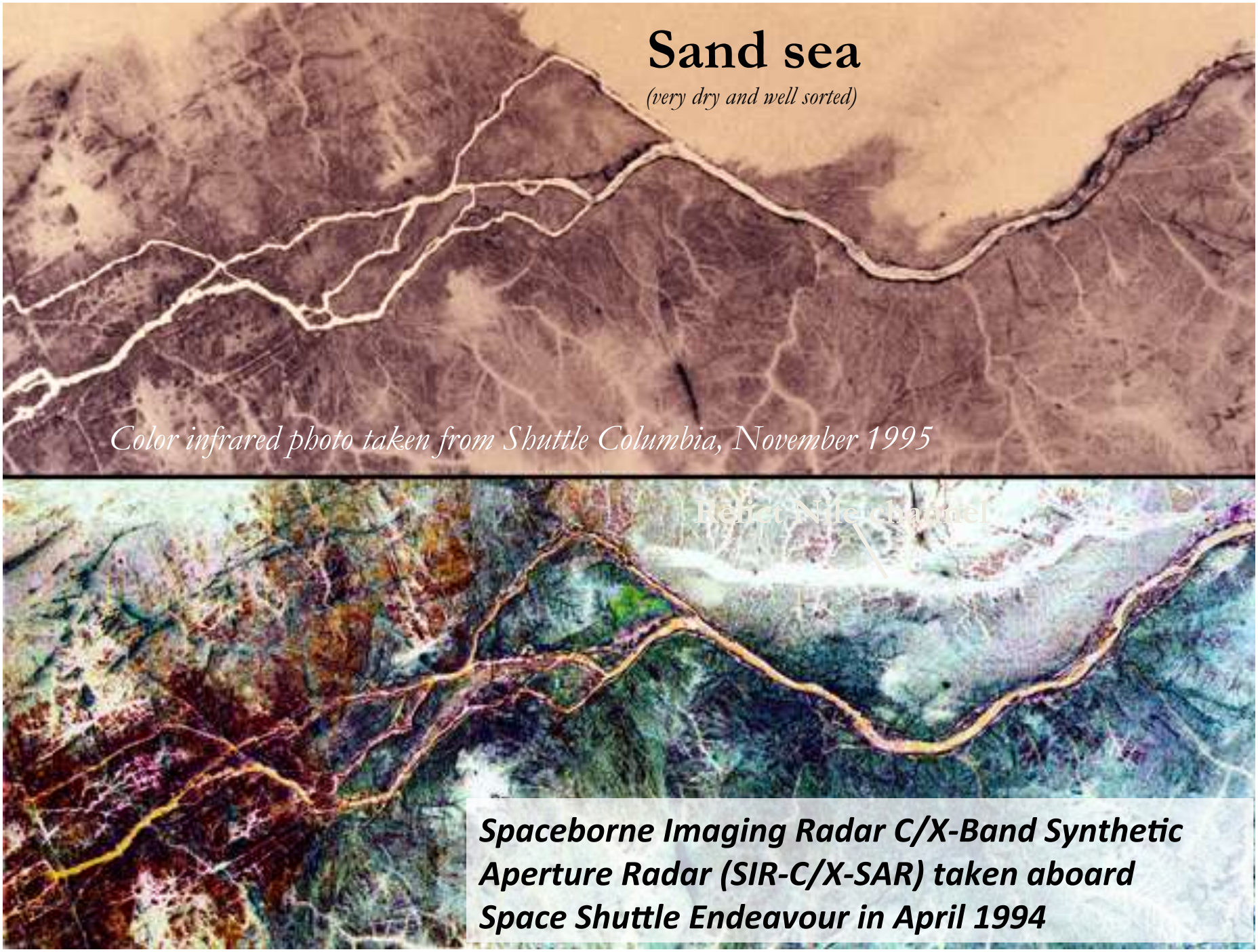
Sand sea
(very dry and well sorted)
Color infrared photo taken from Shuttle Columbia, November 1995
Relict Nile channel
Spaceborne Imaging Radar C/X-Band Synthetic Aperture Radar (SIR-C/X-SAR) taken aboard Space Shuttle Endeavour in April 1994

Example of Radar Penetration from the Sahara

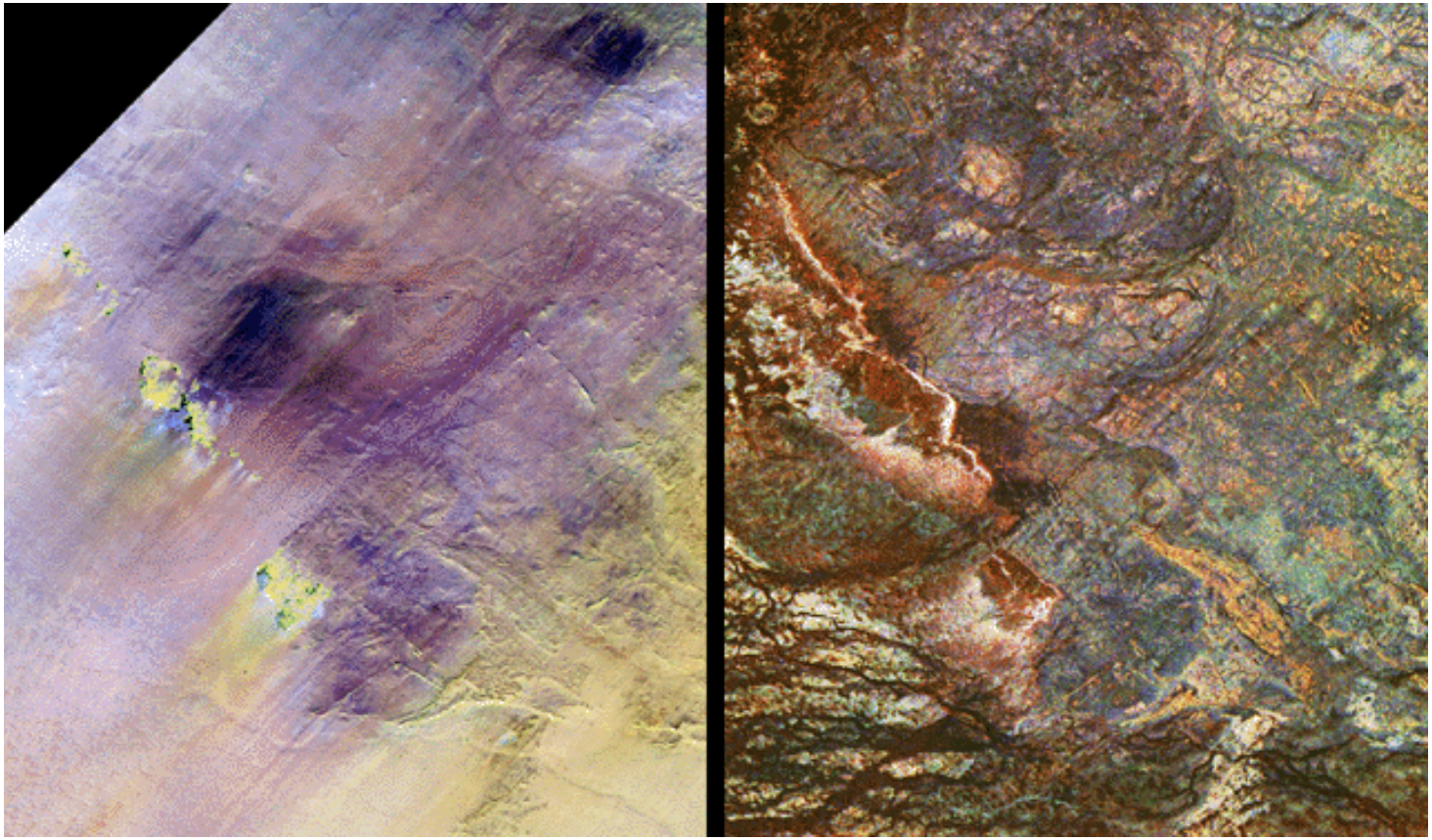

R-Lhh
G-Chh
B-Chv

TM image

Radar image

Example of Radar Bathymetry

Figure 8.34 English Channel near the Strait of Dover: (*a*) Seasat SAR image, L band, midsummer; (*b*) map showing ocean bottom contours in meters. (Courtesy NASA/JPL/Caltech.)

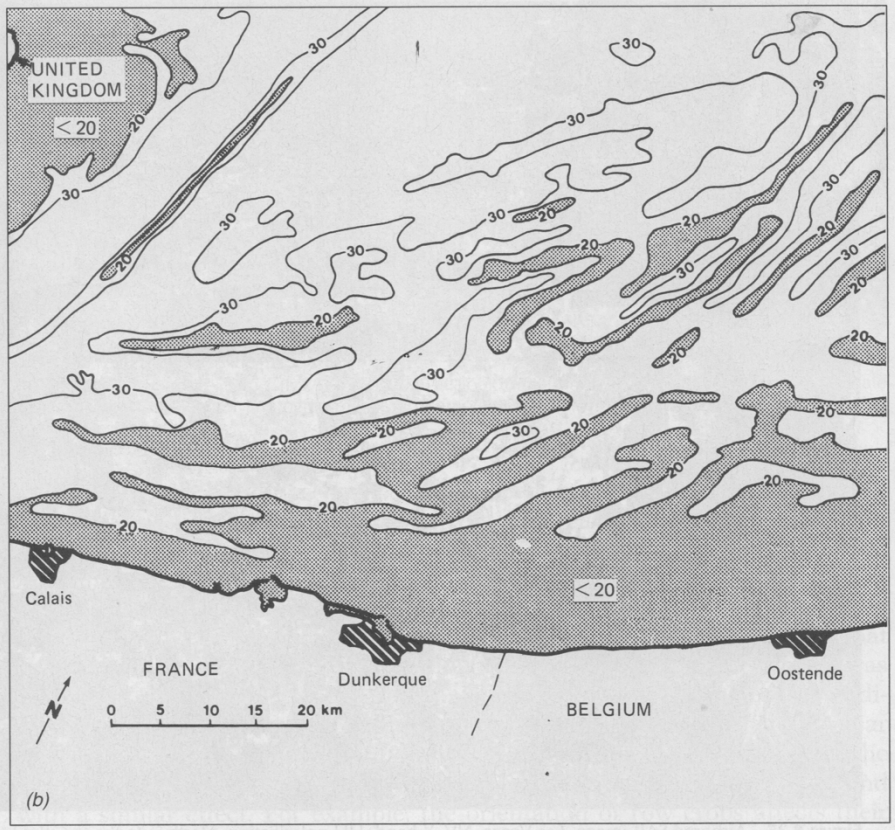

Figure 8.34 *(Continued)*

SAR Imaging Radar Experiments

	Seasat	*SIR-A*	*SIR-B*	*SIR-C*	*ERS-1*	*JERS-1*	*Almaz*	*Magellan*	*Radarsat*
Launch date	1978	1981	1984	1994	1991	1992	1991	1989	1995
Wavelength, cm	23.5 (L)	23.5 (L)	23.5 (L)	3.0 (X) 6.0 (C) 24.0 (L)	5.7 (C)	23.5 (L)	9.6 (S)	12.6 (S)	5.7 (C)
Depression angle	70°	40°	30 to 75°	Variable	67°	55°	40 to 58°	65°	40 to 70°
Spatial resolution, m	25	38	25	Variable	218	18	15	100	Variable
Polarization	HH	HH	HH	Multiple	VV	HH	HH	HH	HH
Swath width	100	50	40	30 to 60	100	75	50 to 100	20	50 to 100
Altitude, km	790	250	225	225	785	568	350	290 to 2000	800
Latitude covered	72°N to 72°S	50°N to 50°S	58°N to 58°S	57°N to 57°S	Polar	Polar	Polar	Polar	Polar
Nationality	USA	USA	USA	USA	Europe	Japan	Russia	USA	Canada

Venus topography and radar brightness (Magellan)

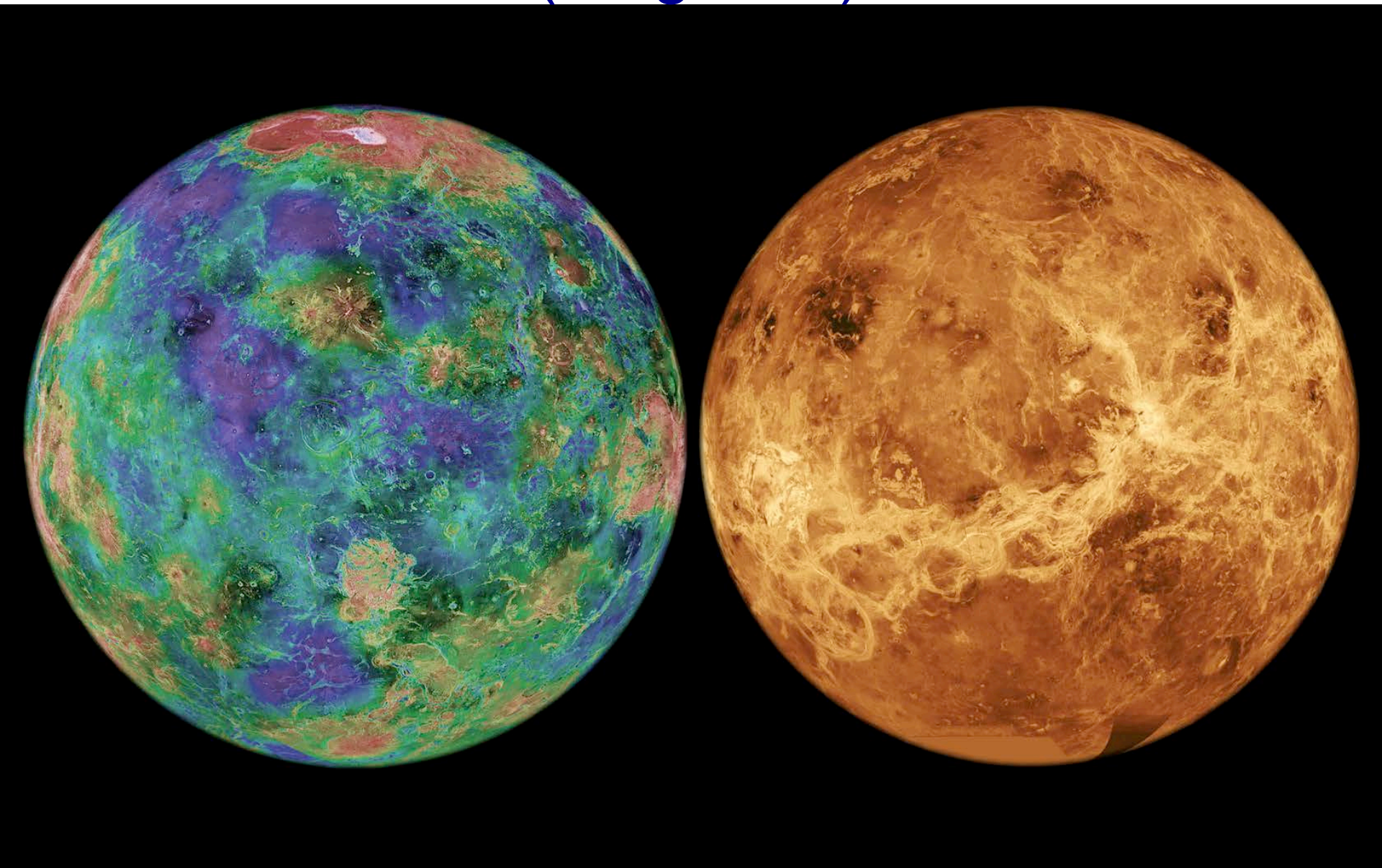

Key Spacecraft Characteristics

- Single radar instrument operates simultaneously (by interleaving) in Synthetic Aperture Radar (SAR), altimeter, and radiometer modes.
- High Gain Antenna (3.7m diameter) is used as both the radar and telecommunications antenna.
- X-band downlink data rate of 268.8 or 115 kbps.
- Coherent X- and S-band radio subsystem used for gravity field measurement by precision tracking of the spacecraft's orbit.
- Spacecraft on-orbit dry mass of 1035 kg.
- Monopropellant hydrazine thruster system (0.9 to 445N thrust).
- Powered by solar panels with rechargeable batteries.
- Three orthogonal electrically powered reaction wheels used for spacecraft pointing control.

Key Radar Characteristics

- Synthetic Aperture Radar (SAR)
  - Frequency: 2.385 GHz
  - Peak Power: 325 W
  - Pulse Length: 26.5 microsec
  - PRF: 4400-5800 Hz
  - Swath Width: 25 km (variable)
  - Data Acquisition Rate: 806 kbps
  - Downlink Quantization: 2 bits
- Operates in SAR, altimeter, and radiometer modes
  - SAR Resolution: 150m range/150m azimuth
  - Altimeter Resolution: 30m
  - Radiometer Accuracy: 2 degree C

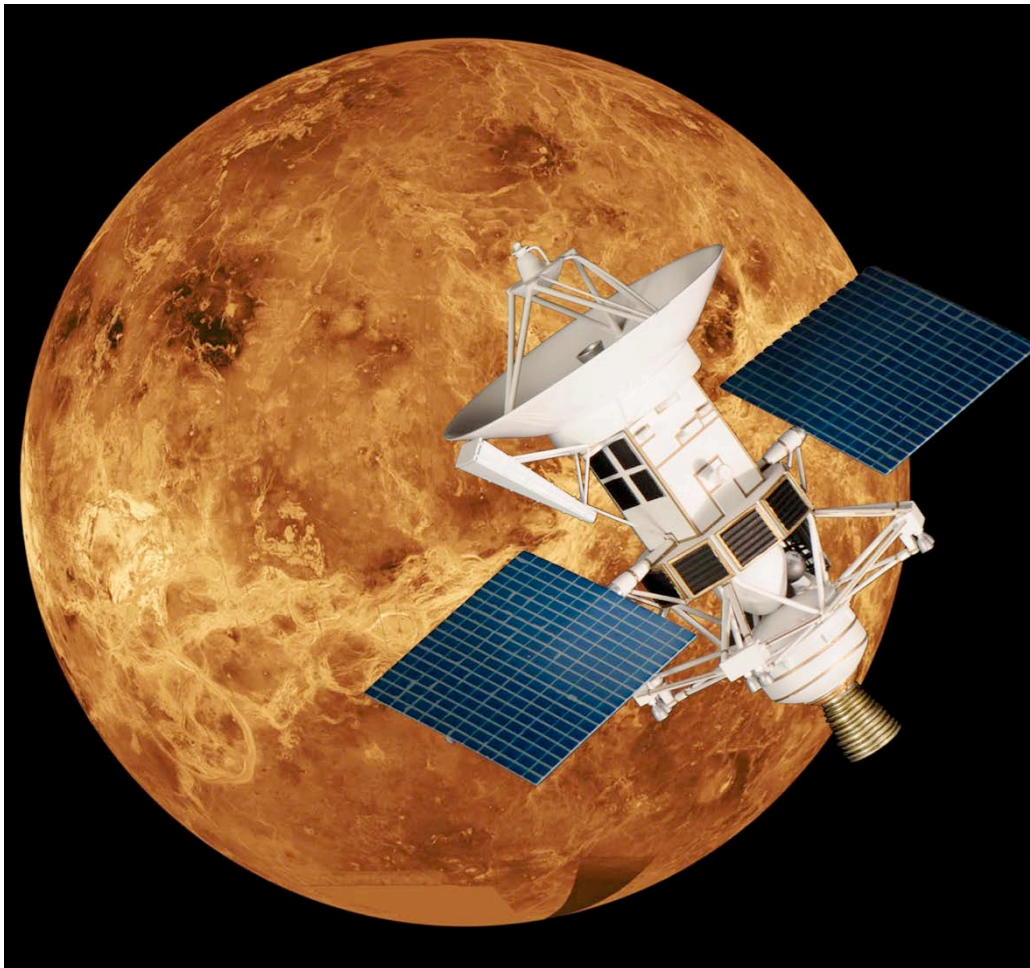

Kallistos Vallis, Venus (Magellan SAR)

Anastomosing channels on Venus (SAR)

Meandering channels (rilles) on Venus

Figure 12. Simple Venusian rille located at ~2°S, 273°18′E, in Phoebe Regio (Magellan Full Resolution synthetic aperture radar (SAR) Map of Venus (FMAP) left-look mosaic). Lava flows that formed this channel emerged from topographic depressions at d, flooding small basins

Planetary Hypsometry

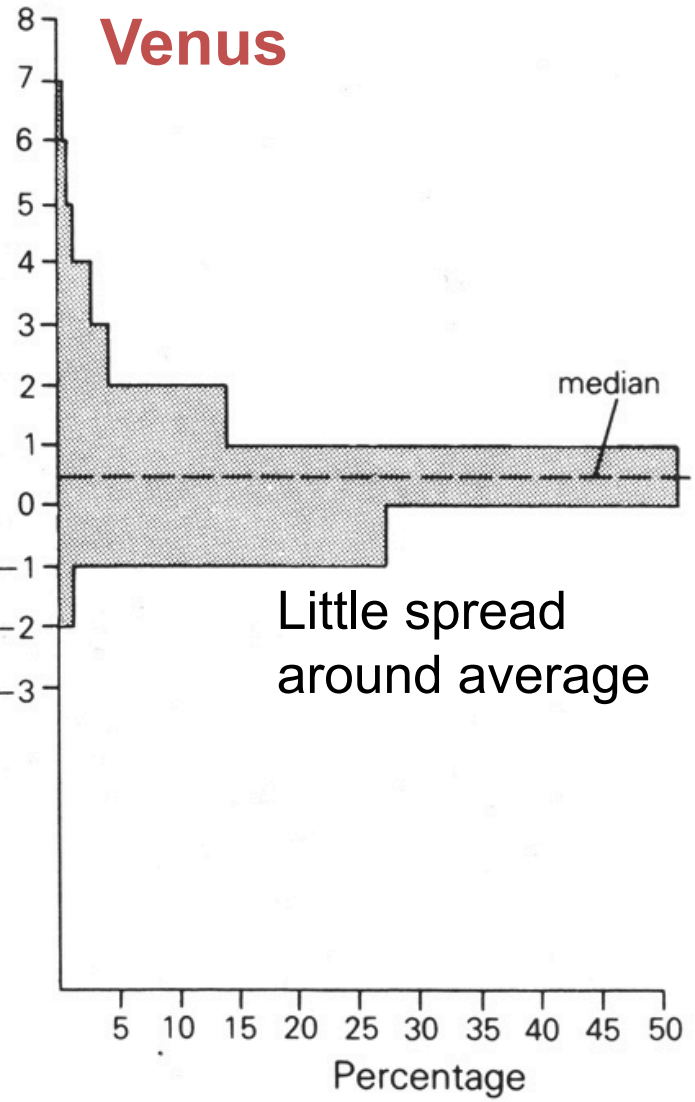

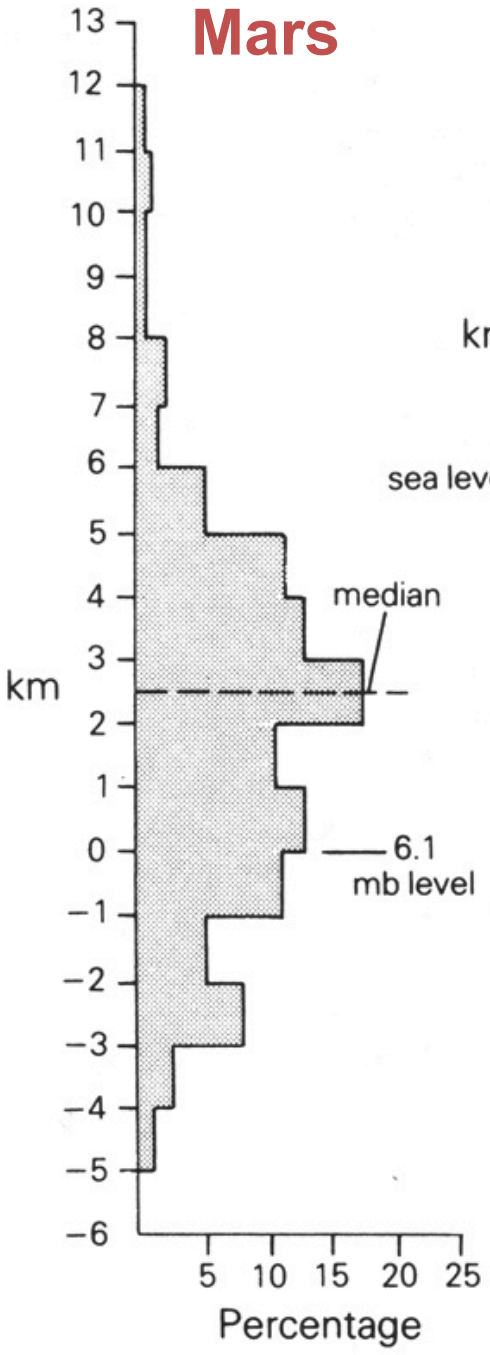

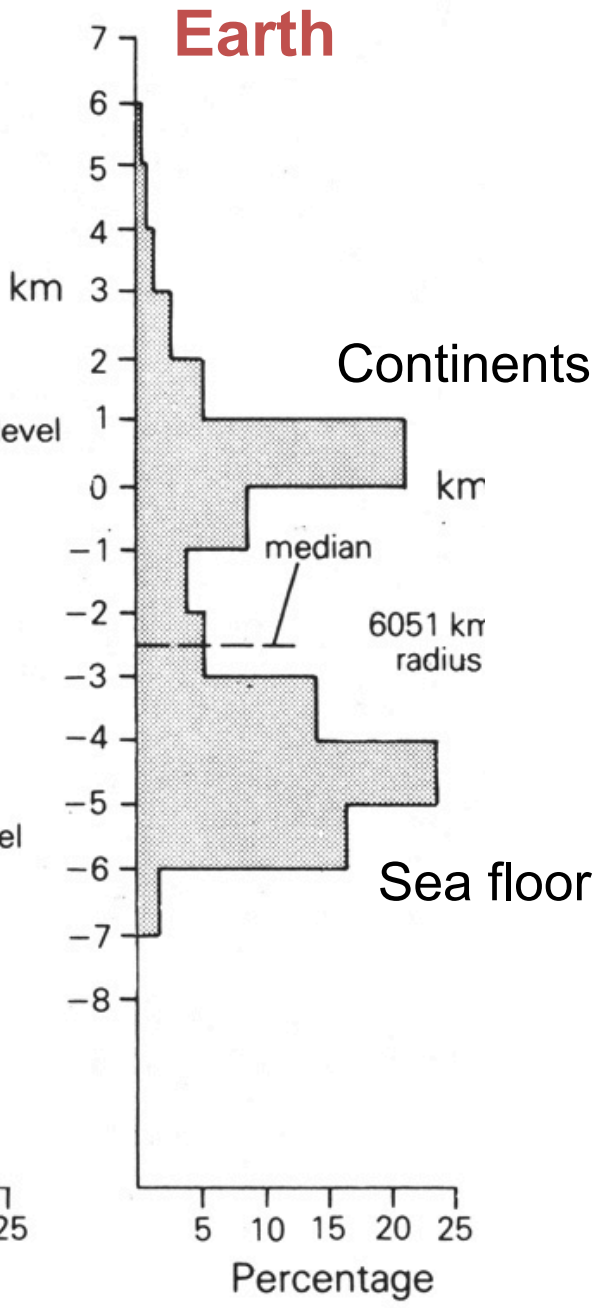


JPL
CASSINI RADAR
CAPABILITY
SURFACE IMAGING
ALTIMETER
RADIOMETER
SCATTEROMETER
TARGETS
TITAN
ICY SATELLITES
SATURN

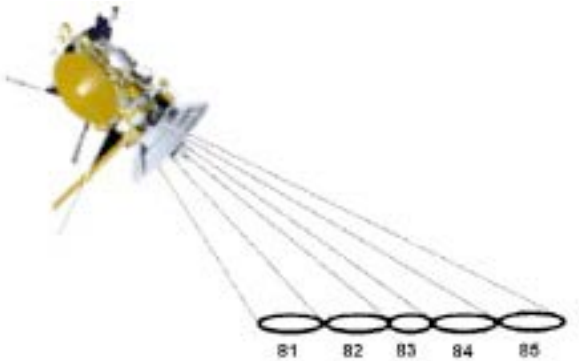
B1
B2
B3
B4
B5

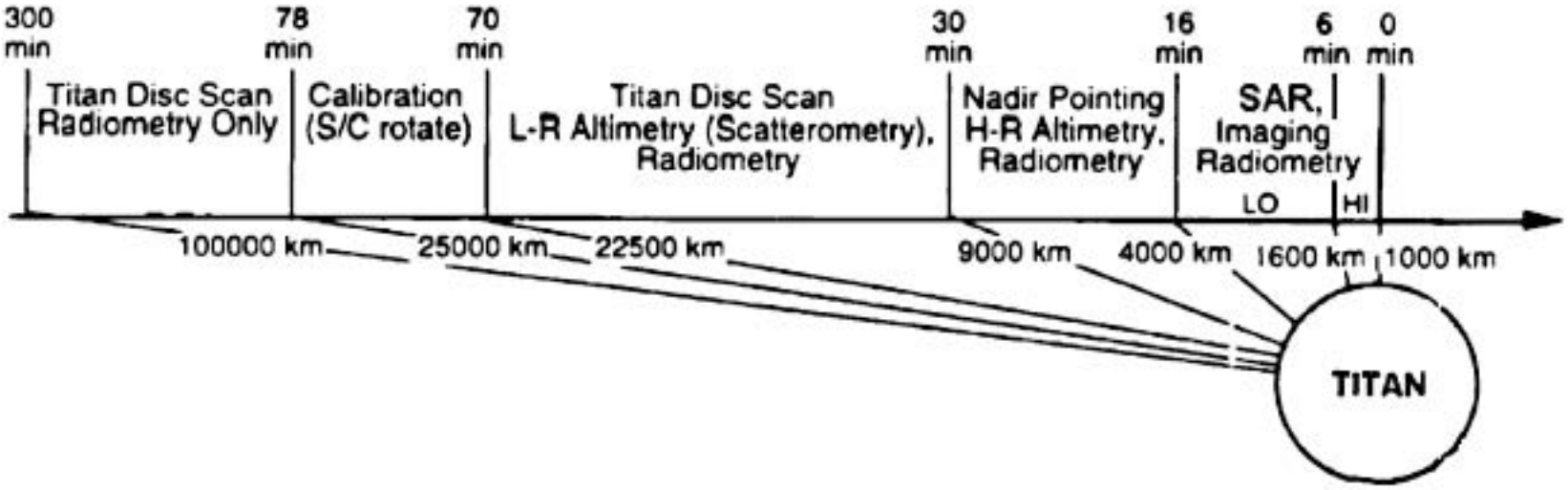
300 min
78 min
70 min
30 min
16 min
6 min
0 min
Titan Disc Scan Radiometry Only
Calibration (S/C rotate)
Titan Disc Scan L-R Altimetry (Scatterometry), Radiometry
Nadir Pointing H-R Altimetry, Radiometry
SAR, Imaging Radiometry
LO
HI
100000 km
25000 km
22500 km
9000 km
4000 km
1600 km
1000 km
TITAN

Cassini's 3-meter antenna

Table 1
Nominal radiometer characteristics

Frequency	13.78 GHz
Wavelength	2.18 cm
Bandwidth	135 MHz
Measurement noise	0.025 K/$\sqrt{\text{Hz}}$
Beamwidth (beam 3)	0.35° × 0.35°
Beamwidths (beam 1, 2, 4, 5)	0.35° (along track) × 1.35° (across track)
Footprint width, beam 3	6 km periapsis, 20 km start/end of SAR
Footprint diameter, beam 1, 2, 4, 5, cross-track	23 km periapsis, 75 km start/end of SAR

Paganelli et al. (2008)

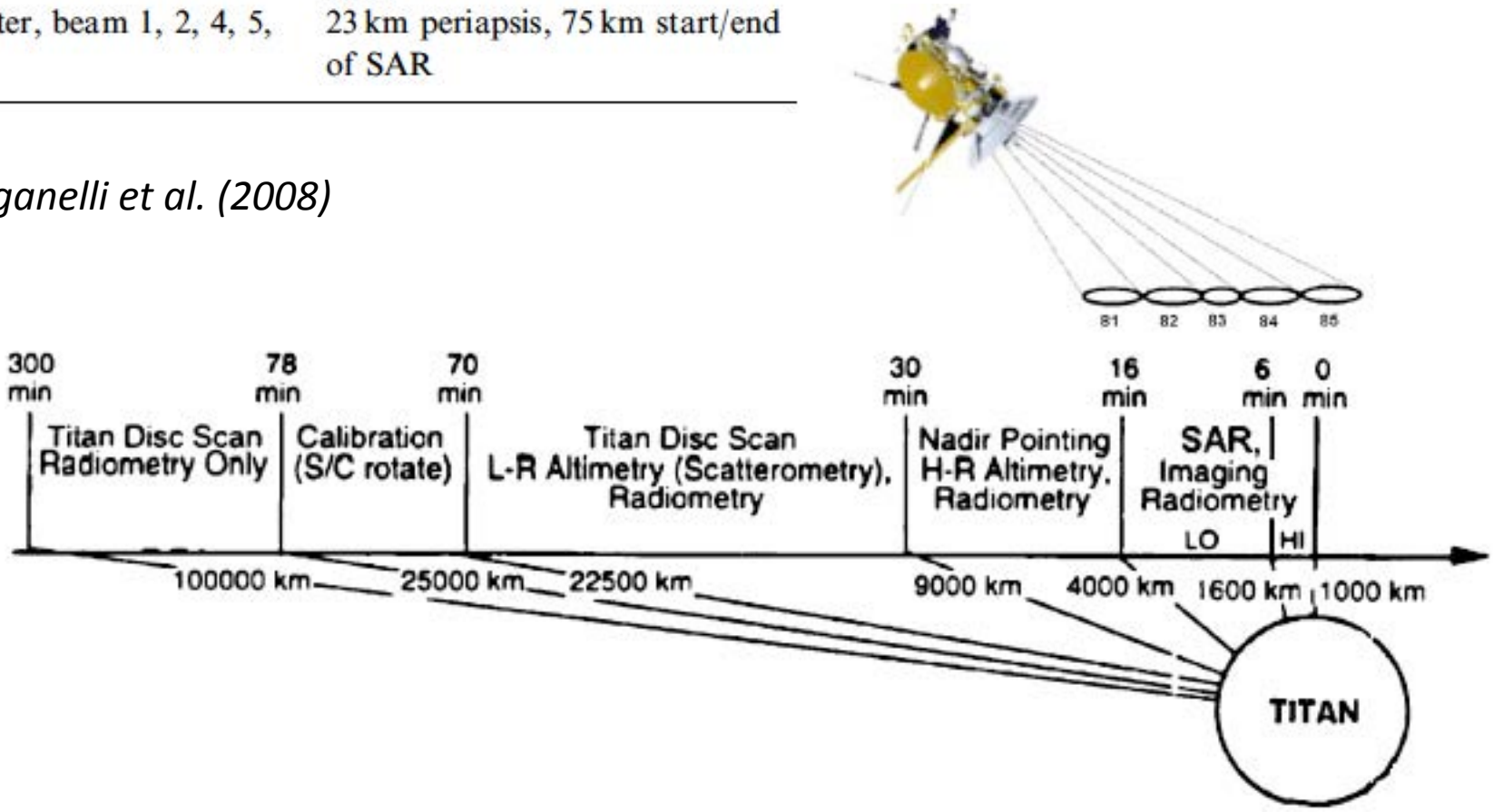

Cassini radar data from Titan

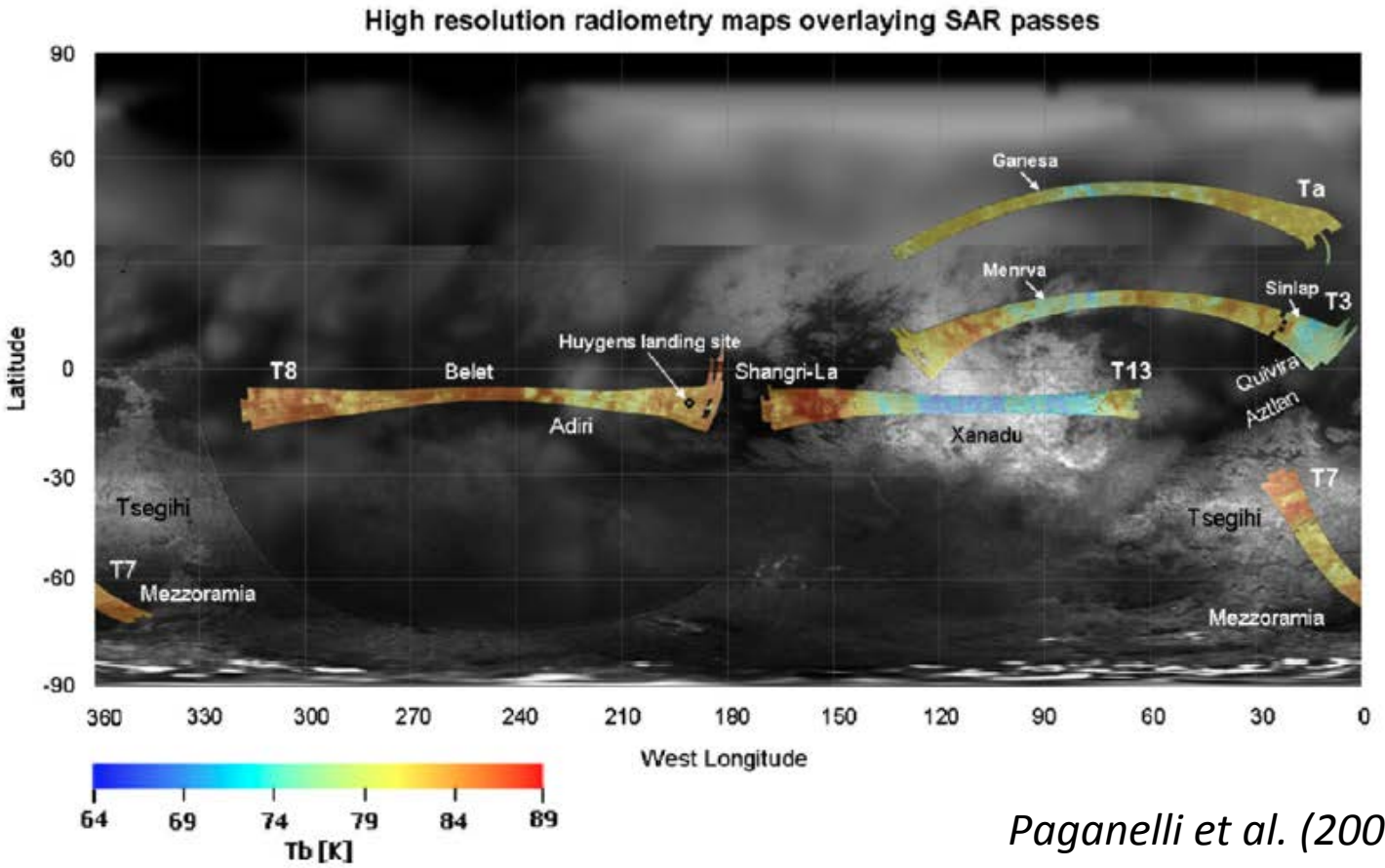

Paganelli et al. (2008)

Fig. 3. Integrated SAR and SAR-radiometry swaths for for Ta, T3, T7, T8, and T13. High-resolution radiometry with transparency level of 60% is overlaid on SAR swaths rendering the anti-correlation between SAR swath and high-resolution radiometry readily apparent while enhancing the characteristics of geological features and associated SAR and radiometry properties. Scale bar for overlaying high-resolution radiometry as in Fig. 2b.

CH_4 Lakes on Titan

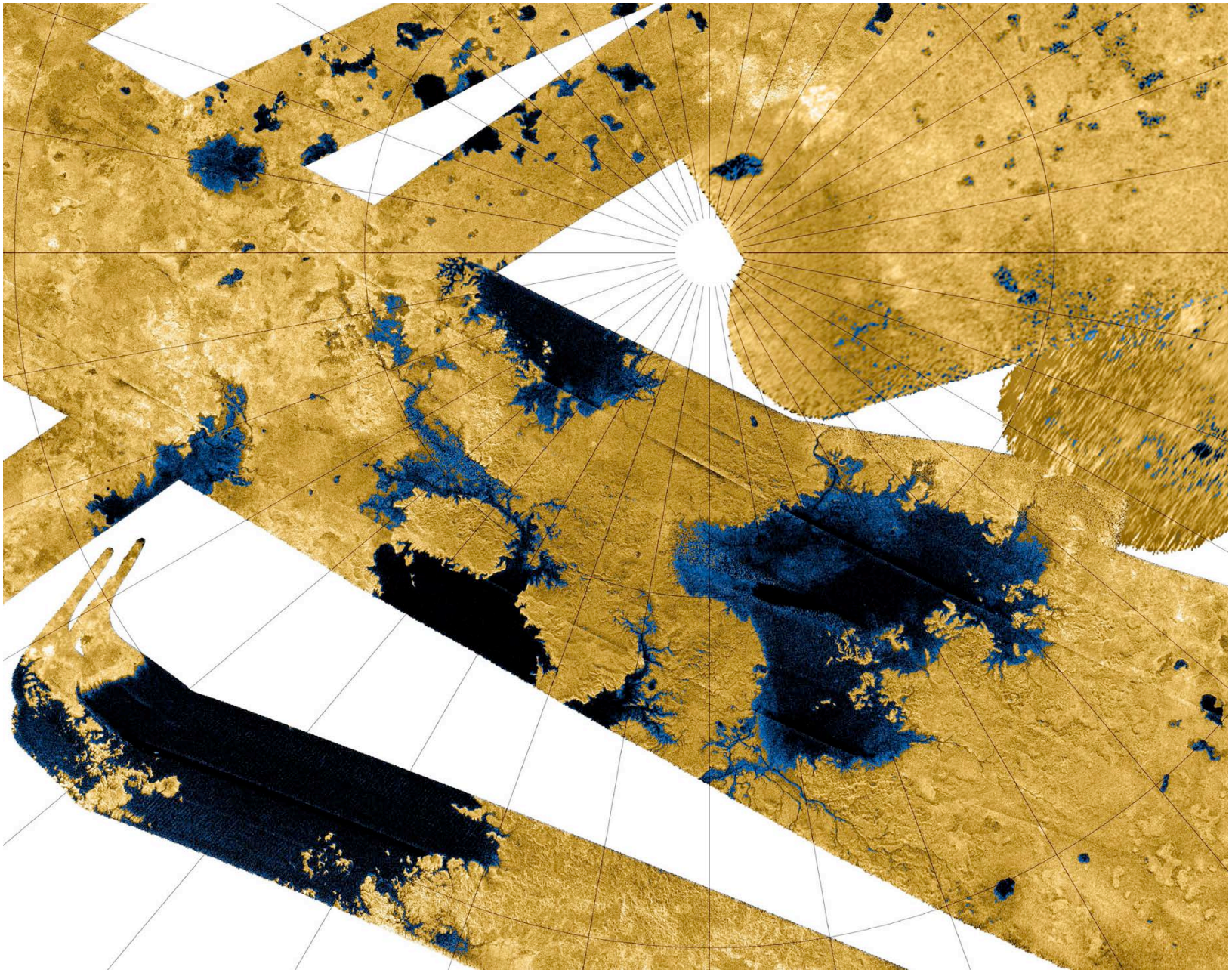

Titan: deep vs. shallow vs. dry lakes

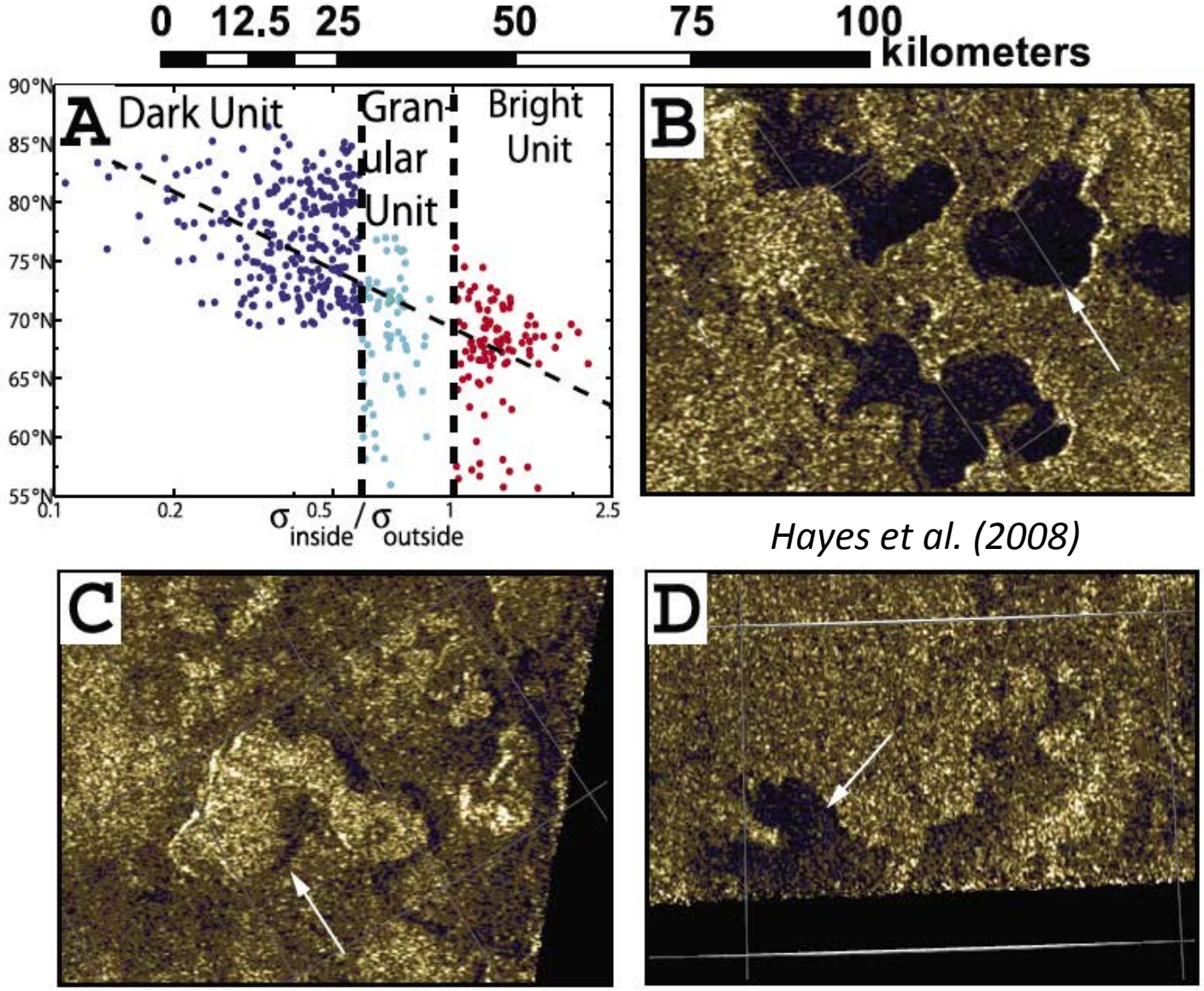

Hayes et al. (2008)

Figure 1. Mapping Units: (a) Ratio between median incidence-angle-corrected off-axis backscatter within and immediately surrounding feature, (b) Dark Unit, (c) Bright Unit, and (d) Granular Unit.

Titan: shoreline bathymetry from backscatter

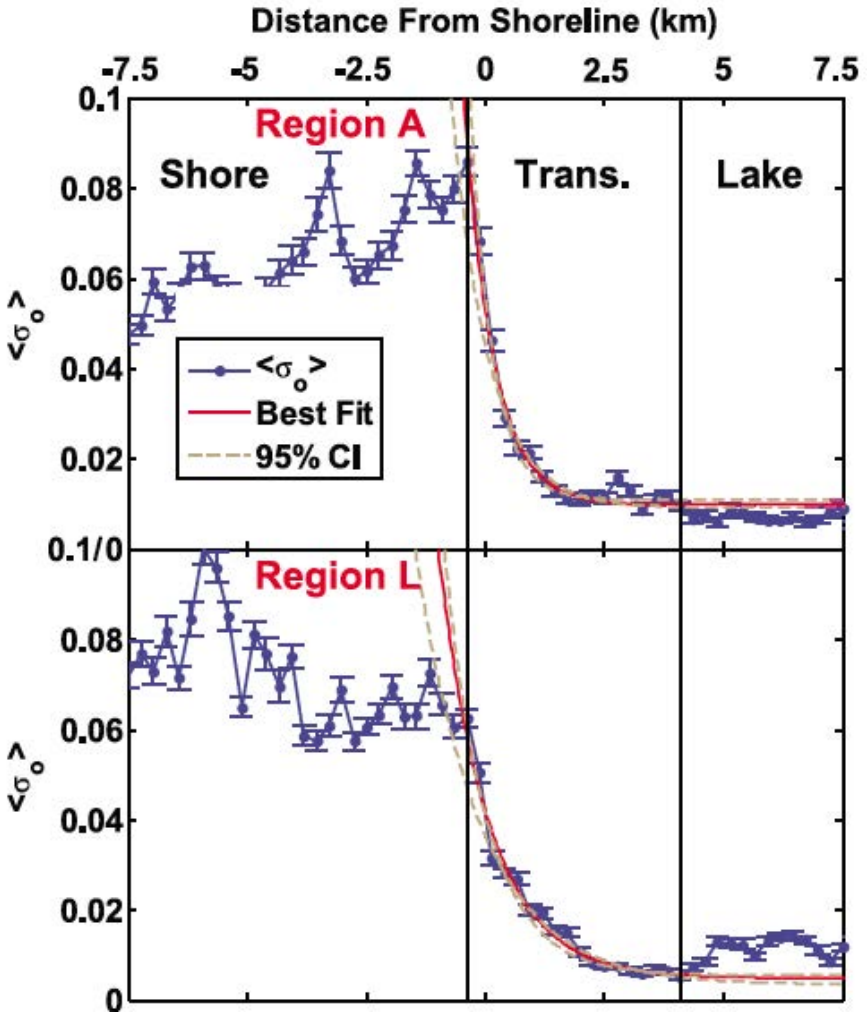

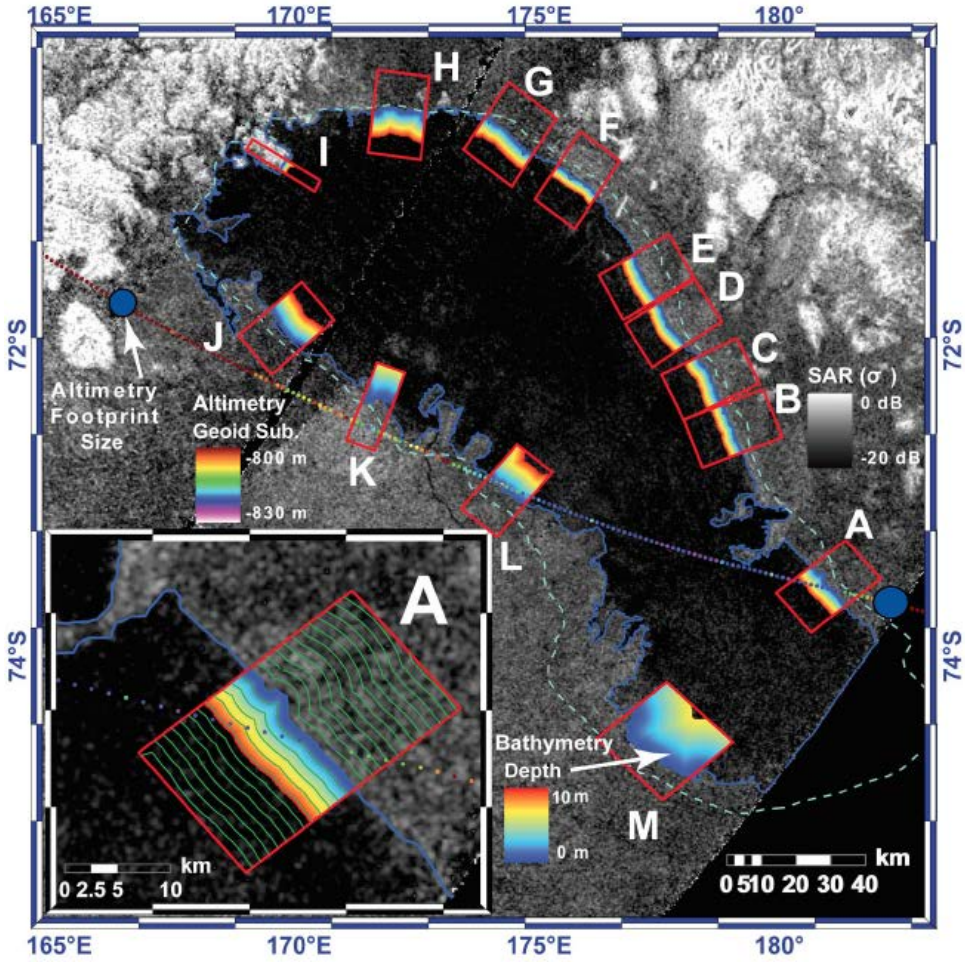

Hayes et al. (2010)

Titan: Cassini radar vs. IR spectral windows

Dunes!

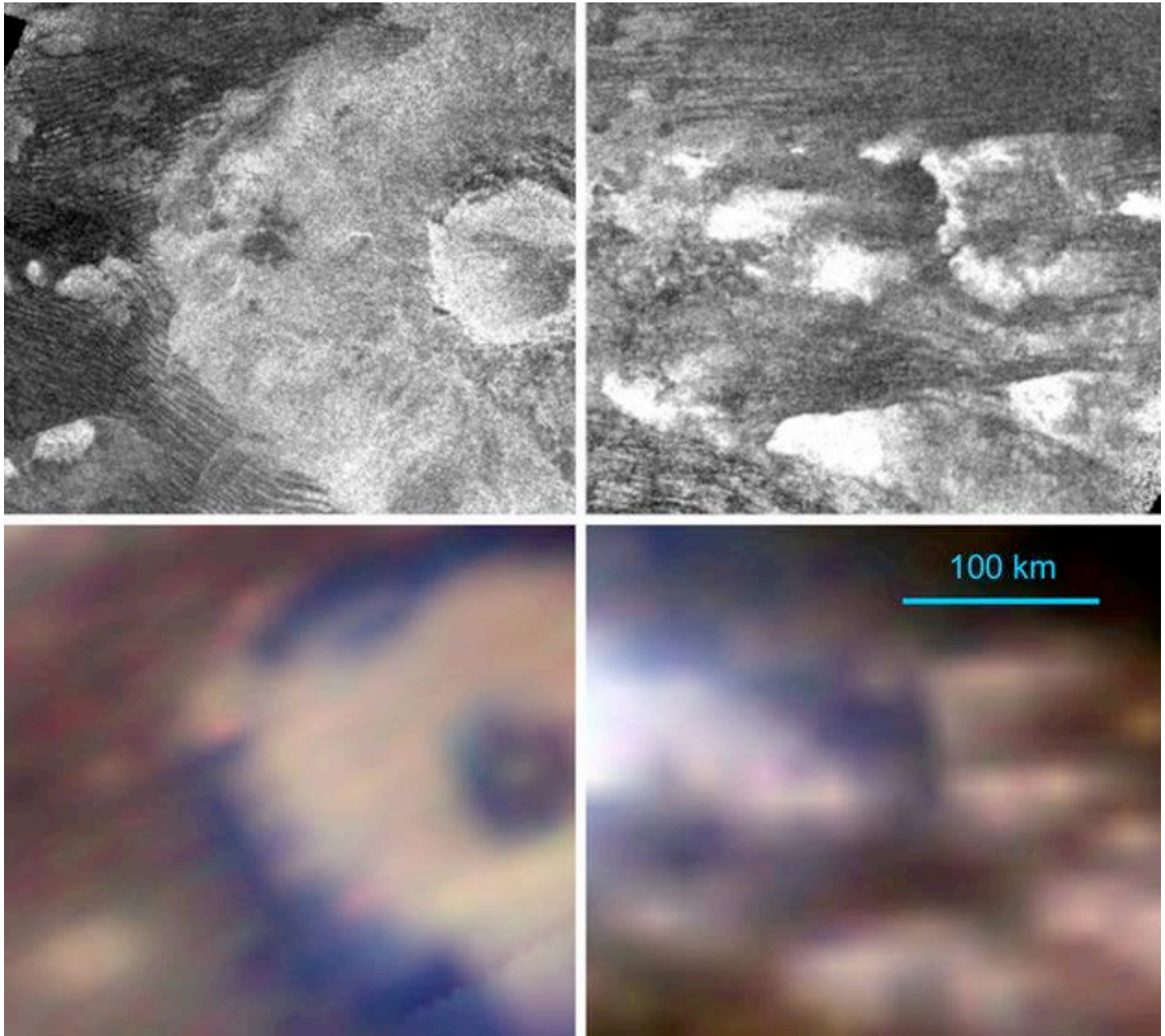

Mars Advanced Radar for Subsurface and Ionospheric Sounding (MARSIS)

MARSIS subsurface sounding mode characteristics				
Centre frequency (MHz)	1.8	3.0	4.0	5.0
Bandwidth (MHz)	1.0	1.0	1.0	1.0
Radiated power (W)	1.5	5.0	5.0	5.0
Transmit pulse width (μS)	250 or 30			
Pulse repetition rate (s^{-1})	130			
Minimum science data rate (kbps)	18			
Maximum science data rate (kbps)	75			

MARSIS ionosphere sounding mode characteristics	
Start frequency (kHz)	100
End frequency (MHz)	5.4
Number of frequencies	160
Transmit pulse length (μS)	91.43
Frequency step (kHz)	10.937
Pulse repetition rate (s^{-1})	130
Sweep duration (s)	7.38

Mars Advanced Radar for Subsurface and Ionospheric Sounding (MARSIS)

"The primary objective is to map the distribution of liquid and solid water in the upper portions of the crust of Mars." [*Picardi et al.*, 2004]

Table 1. Dielectric properties of the subsurface material.

	Crust Material		*Pore-Filling Material*	
	Andesite	*Basalt*	*Water Ice*	*Liquid Water*
ε_r	3.5	7.1	3.15	88
tan δ	0.005	0.014	0.00022	0.0001

Recall: Interaction of light with materials

relative electric permittivity $\varepsilon_r = \varepsilon/\varepsilon_0$

a.k.a. ***dielectric constant***

Absorptive materials have a *complex* dielectric constant

$$\varepsilon_r = \varepsilon' - i\varepsilon''$$

$$= \varepsilon'(1 - i\tan\theta)$$ for ***loss tangent*** $\tan\theta$

This, in turn, makes $n = \sqrt{(\varepsilon_r)}$ complex …

Martian polar caps

Mostly* H_2O, seasonal CO_2 cover

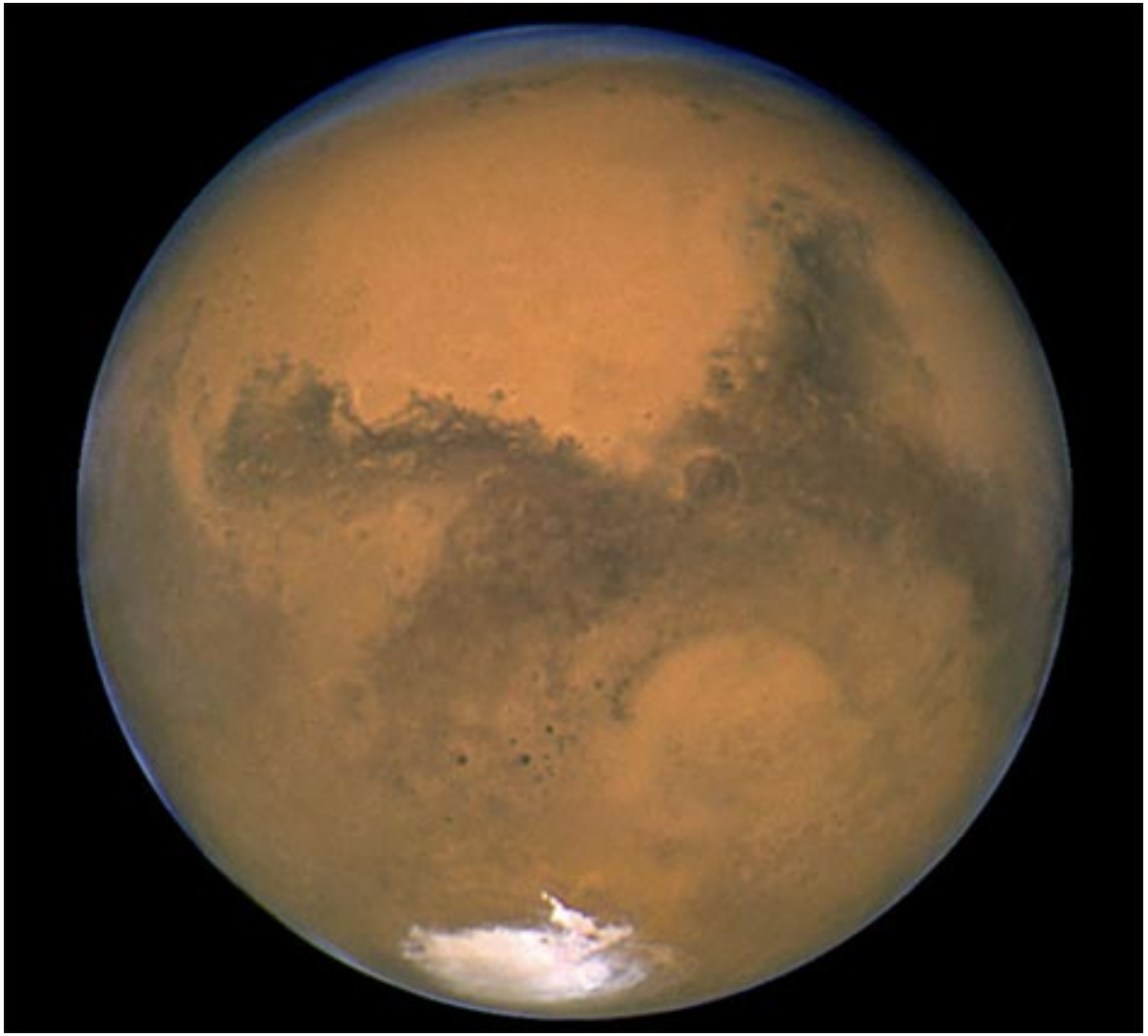

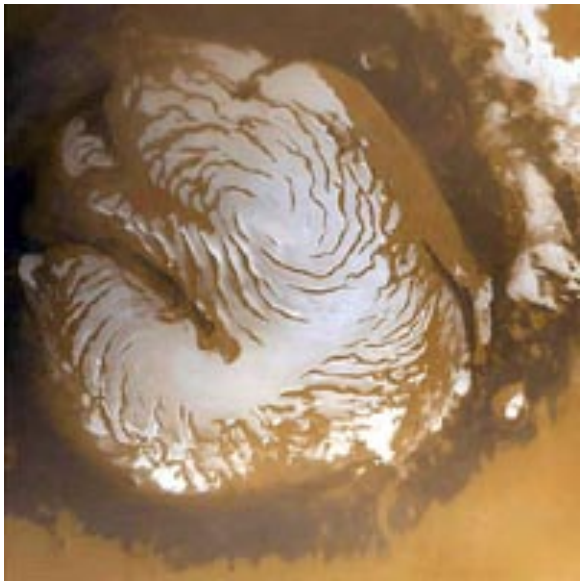

MARSIS view: north polar layered deposits

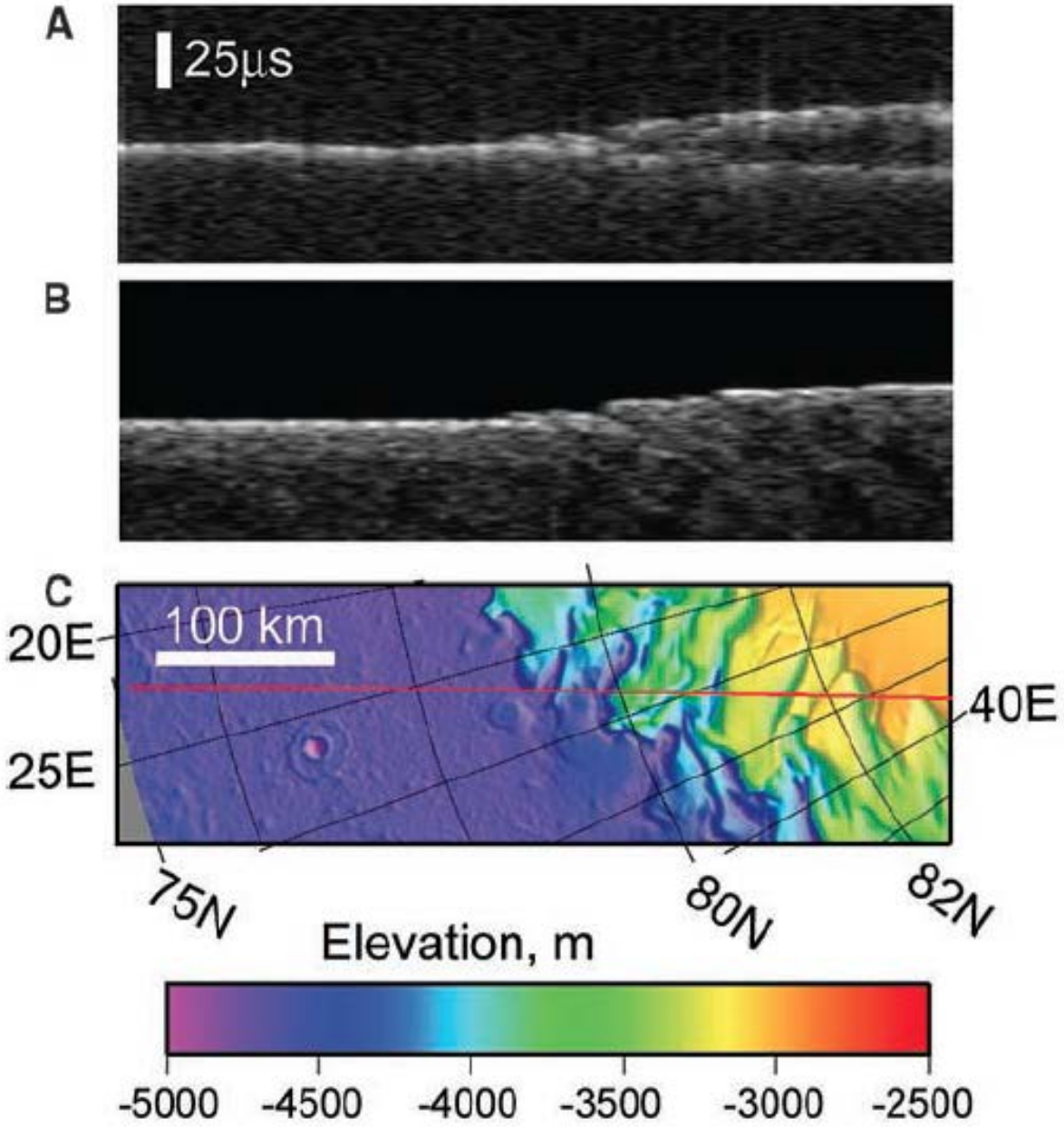

Fig. 1. (A) MARSIS data in radargram format for orbit 1855 as it crossed the margin of the NPLD. (B) Simulated MARSIS data if echoes are only from the surface (nadir and off-nadir clutter). (C) MOLA topography along the ground track (red line); elevation is relative to mean planetary radius. MARSIS data at 5 MHz show a split of the strong return into two as the ground track reaches the NPLD (higher terrain to the right). Maximum time delay to the second reflector is 21 μs, equivalent to 1.8-km depth in water ice.

Picardi et al. (2005)

MRO's Shallow Radar (SHARAD)

Table 2. SHARAD and MARSIS Instrument Parameters

	SHARAD	MARSIS
Frequency band	15–25 MHz chirp	1.3–2.3 MHz, 2.5–3.5 MHz, 3.5–4.5 MHz, 4.5–5.5 MHz chirps
Vertical resolution, theoretical, reciprocal bandwidth, $\varepsilon_r = 4$	7.5 m	75 m
Transmitter power	10 W	10 W
Pulse length	85 μs	250 or 30 μs
PRF	700/350 Hz	127 Hz
Antenna	10-m tip-to-tip dipole	40-m tip-to-tip dipole
Postprocessor SNR (worst-best)	50–58[a] dB	30–50[b] dB
Horizontal resolution (along track × cross track)	0.3–1 km × 3–6 km	5–10 km × 10–30 km

[a]Estimate.
[b]Actual.

Polar Caps: Radar & Interior Structure

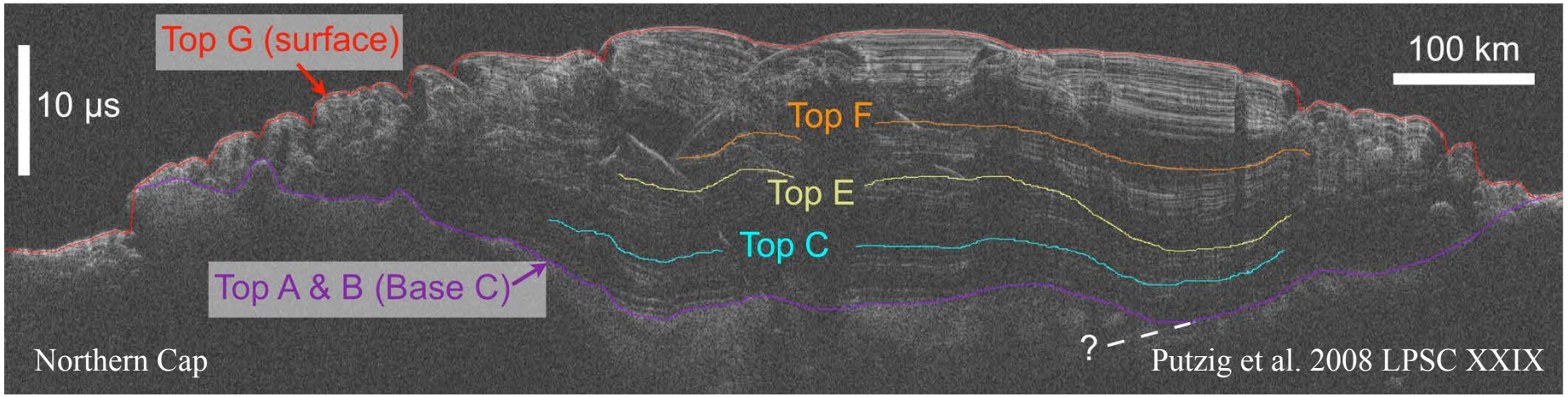

Data from MRO SHARAD.

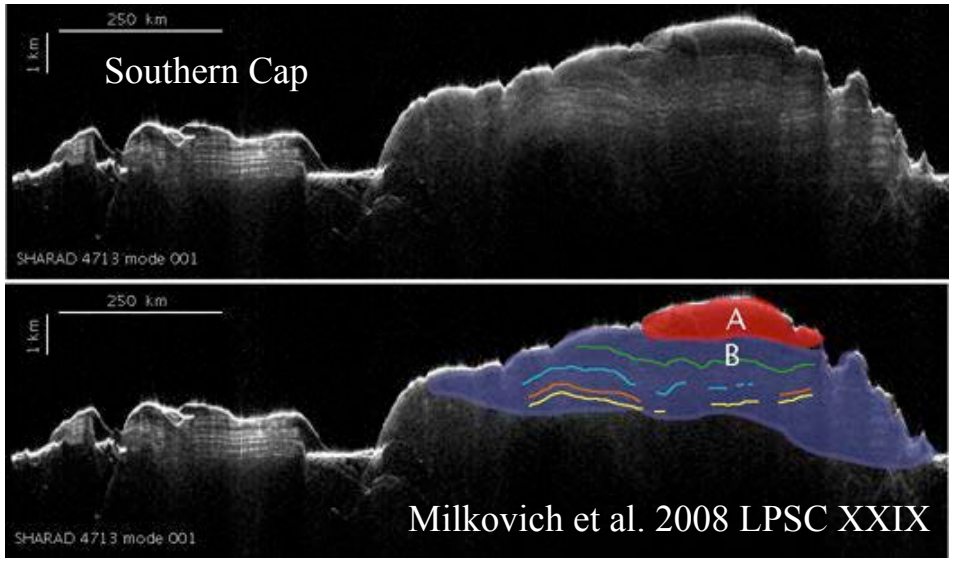

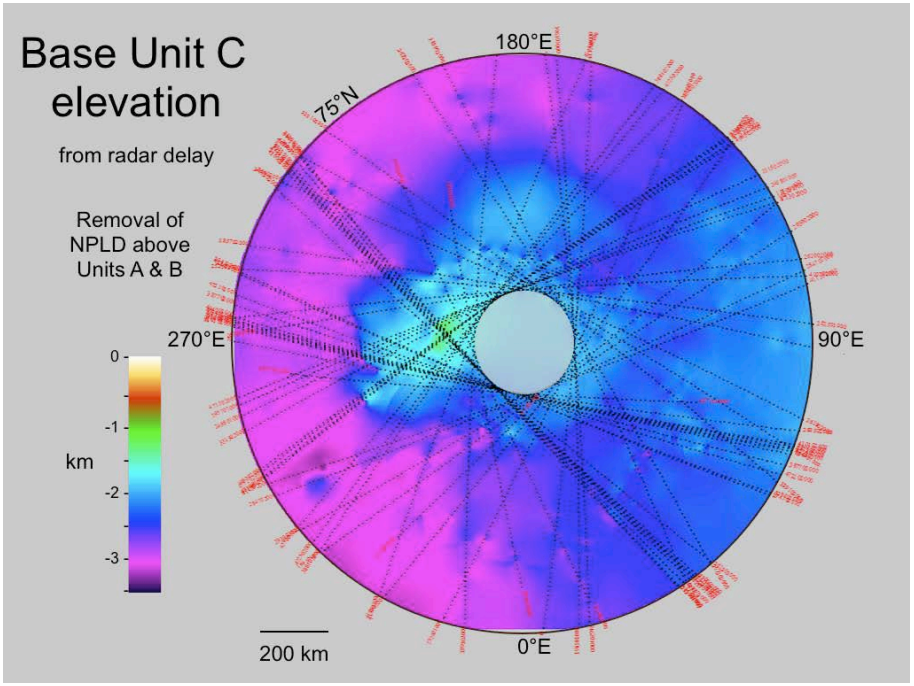

Mars: ground (ice)-penetrating radar

N.E. Putzig et al. / Icarus 204 (2009) 443–457

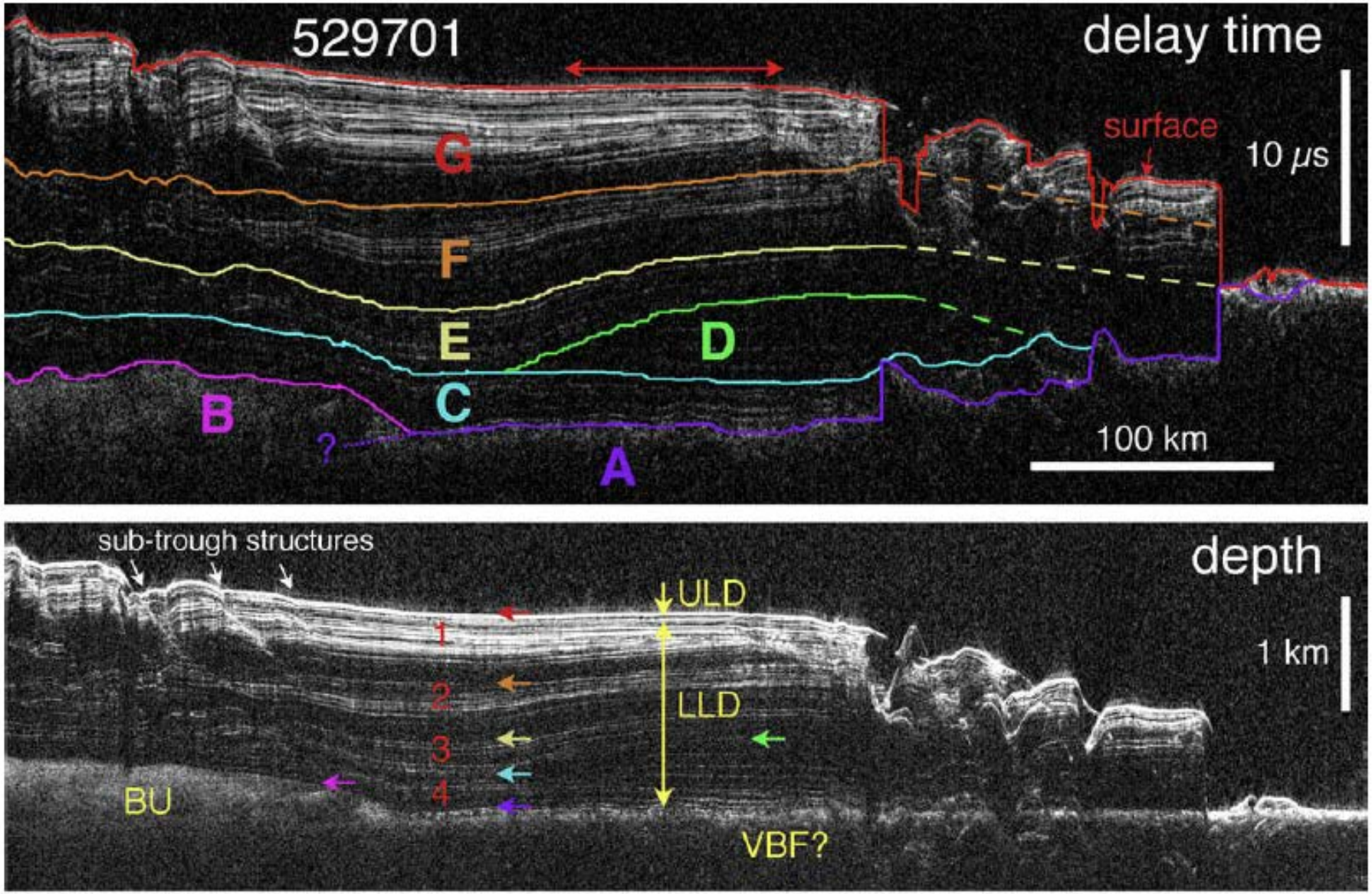

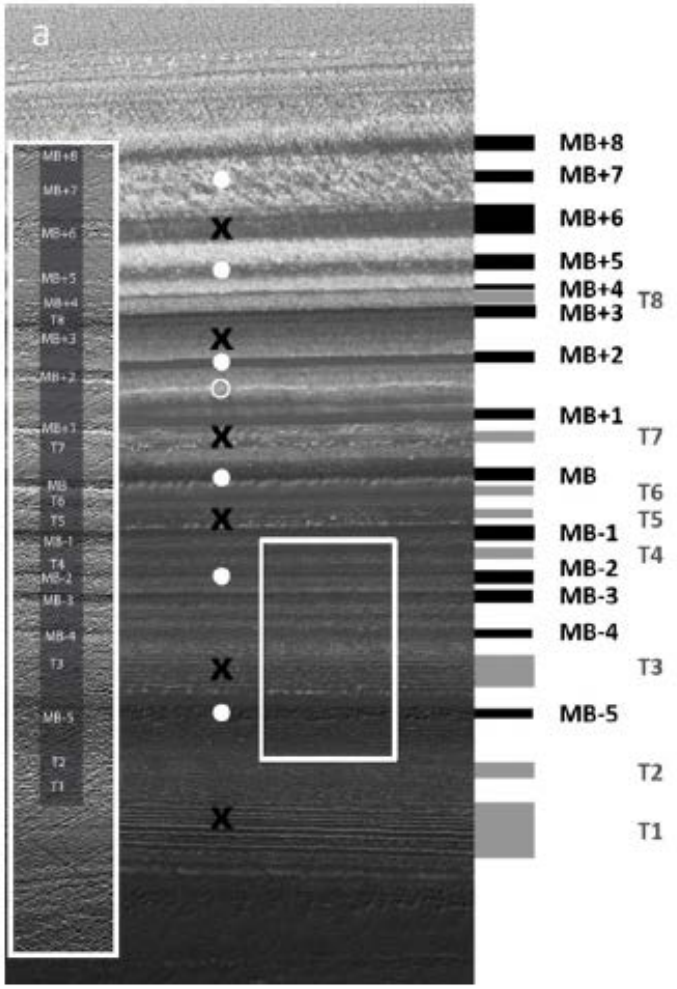

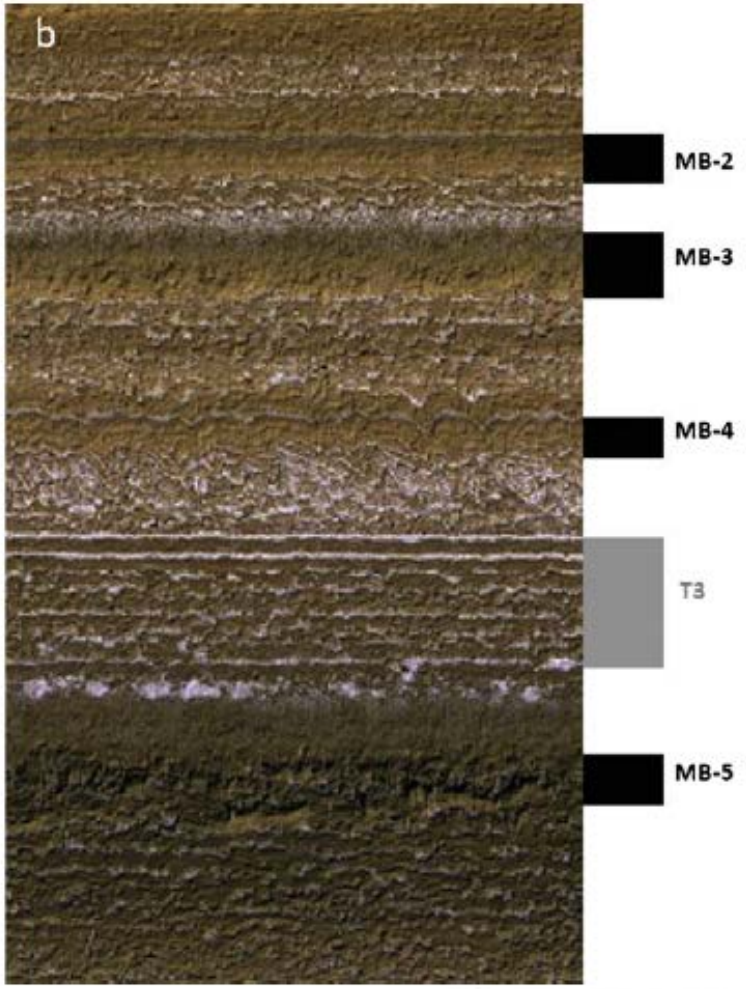

Hvidberg et al. (2012)

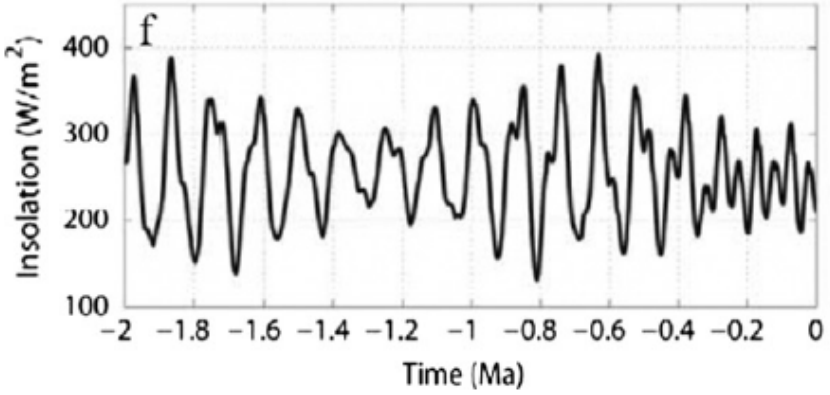

Can compare RADAR view to visible images, climate history models

Mapping mid-latitude ice

Fig. 1. (**A**) Topography of Mars (*24*). Major features are identified, and latitude bands exhibiting lobate debris aprons (LDAs) and lineated valley fill are highlighted (*1*, *2*). The location of our study area along the eastern rim of the Hellas impact basin is also denoted. (**B**) Topography of study area, with MRO/SHARAD ground tracks shown for orbits 6830 (a-a′), 7219 (b-b′), and 3672 (c-c′). LDAs crossed by these tracks are labeled.

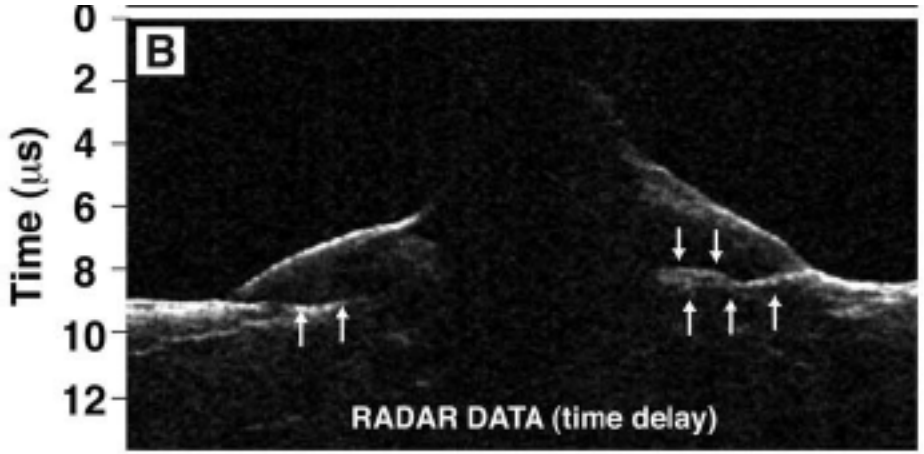

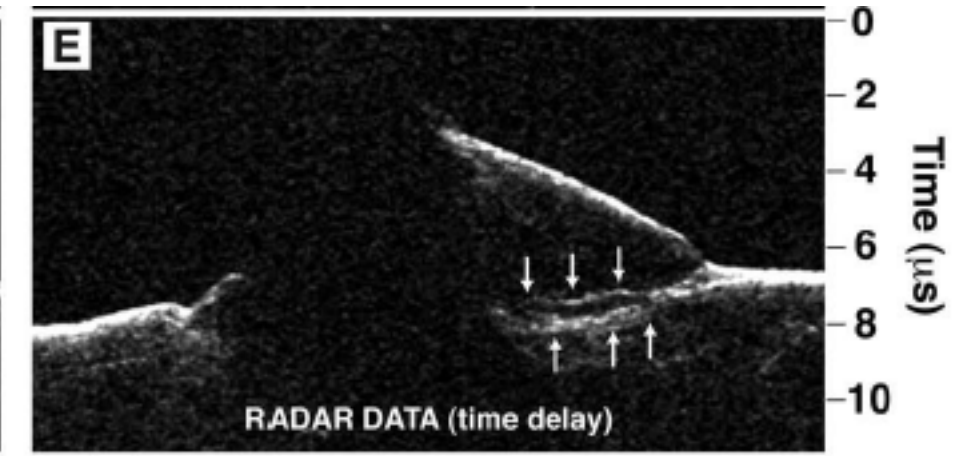

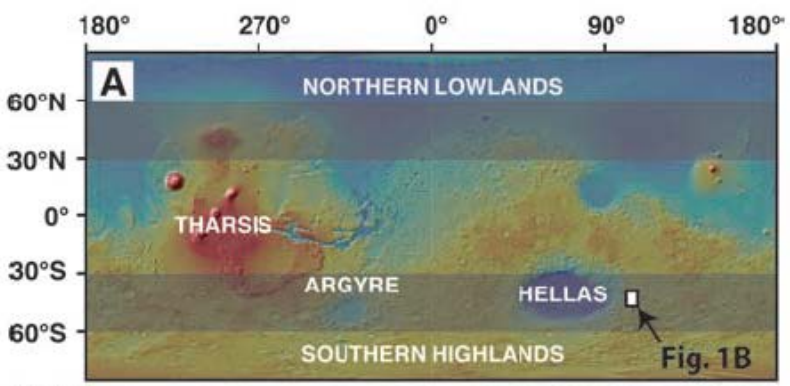

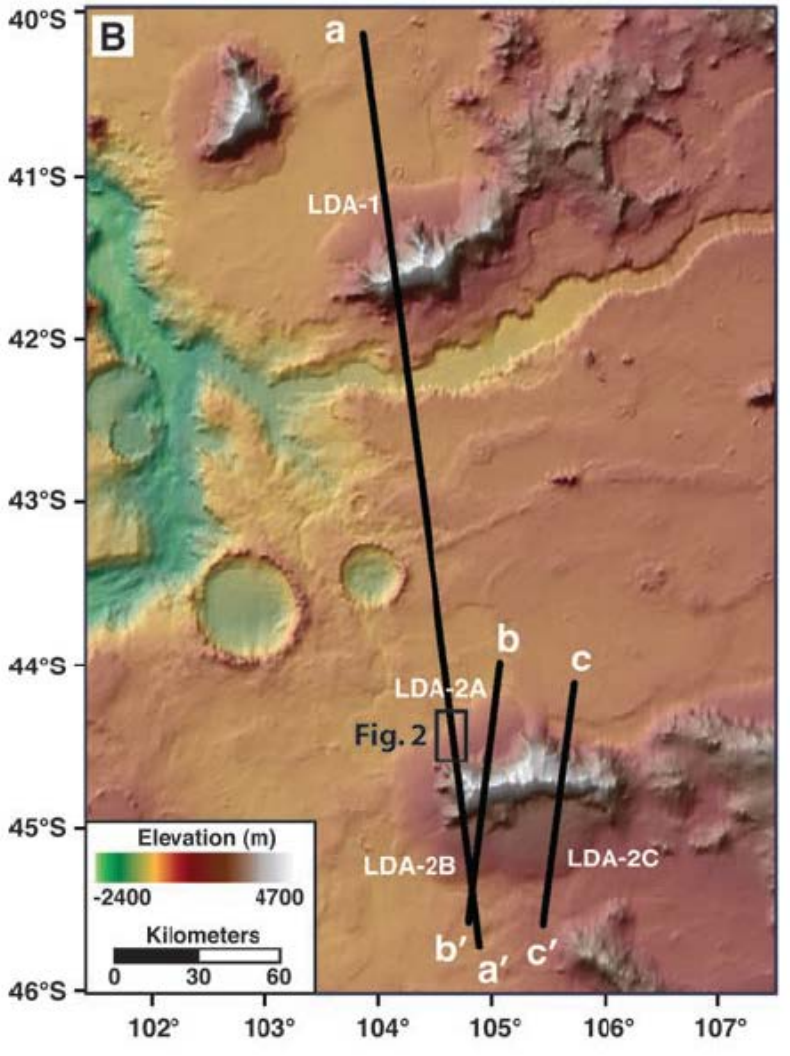

Ground-based planetary radar facilities

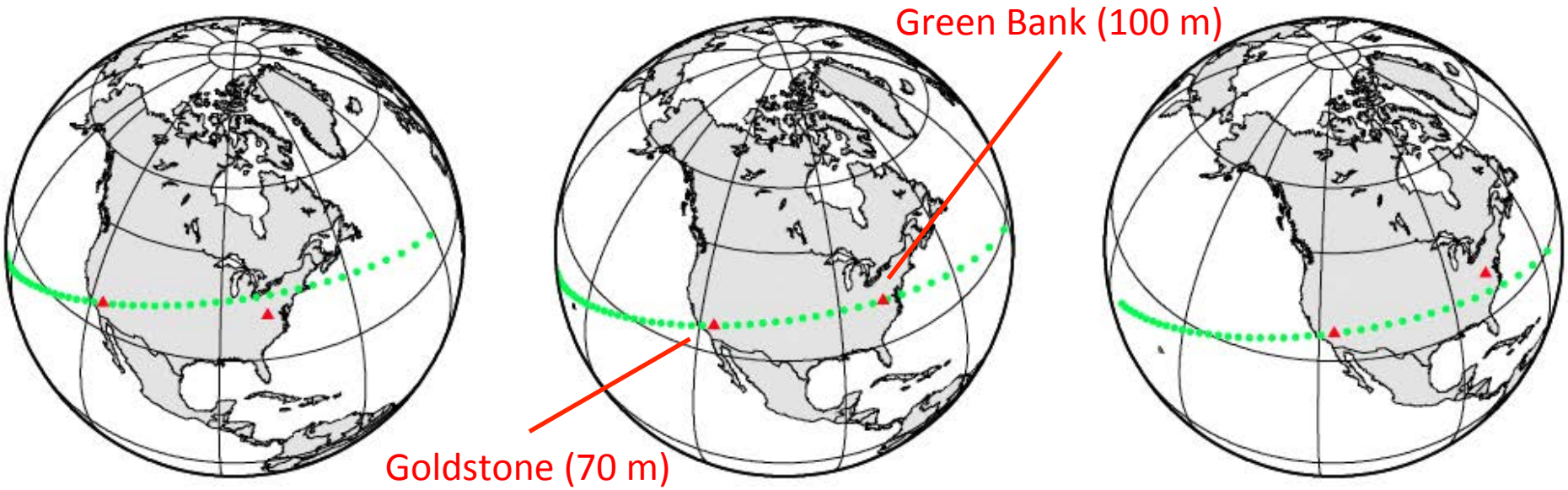

Figure 1. Radar echoes from Mercury sweep over the surface of the Earth during the 2002 May 23 observations. Diagrams show the trajectory of the speckles one hour (left) before, (middle) during, and (right) one hour after the epoch of maximum correlation. Echoes from two receive stations (red triangles) exhibit a strong correlation when the antennas are suitably aligned with the trajectory of the speckles (green dots shown with a 1 s time interval).

- Arecibo (305 m), Goldstone are the only two that transmit
- *Margot et al.* (2007) inferred Mercury has molten core

Radar Delay-Doppler Mapping of Asteroids

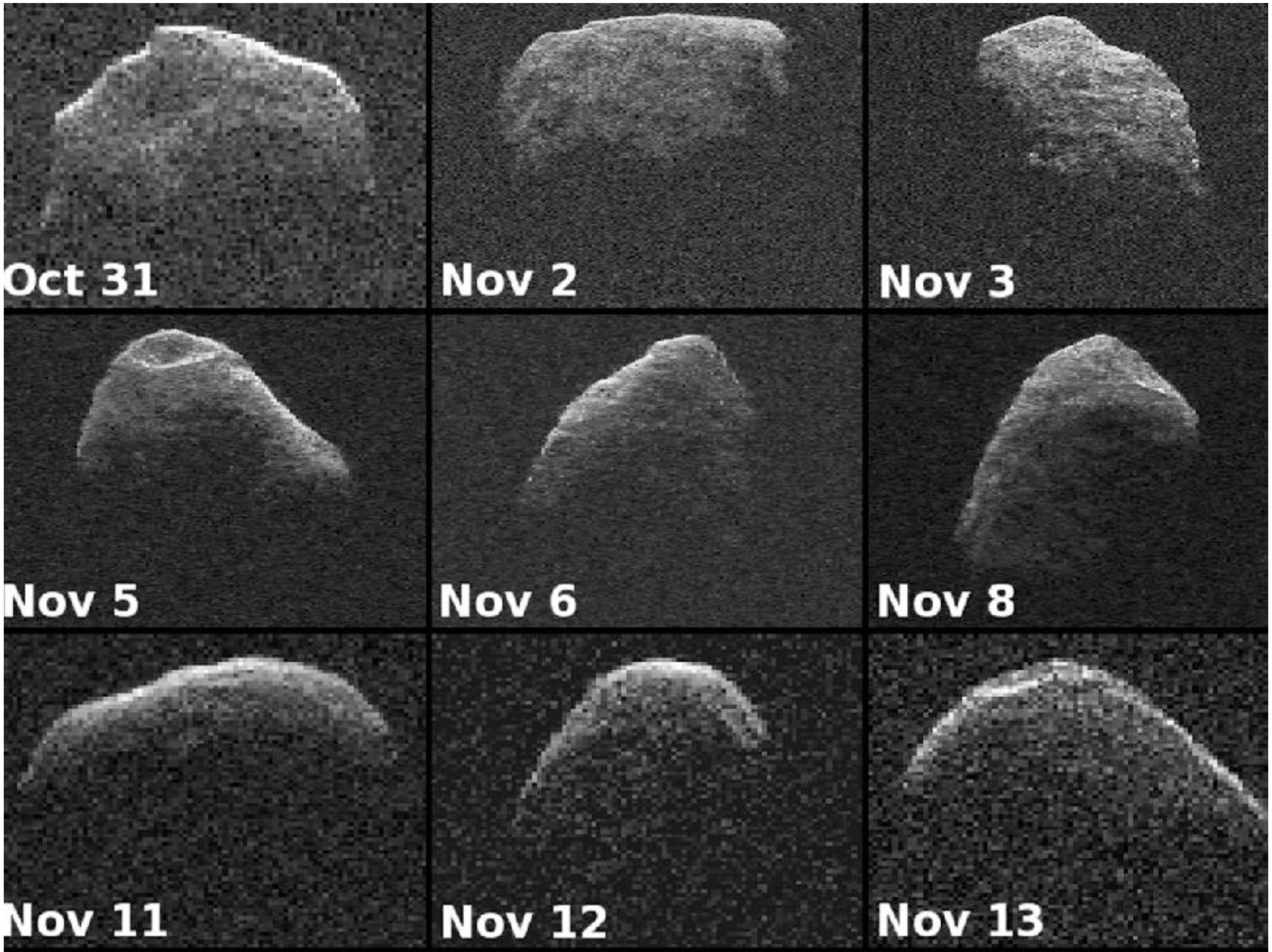

“Contact Binary” Asteroid 2005 CR37

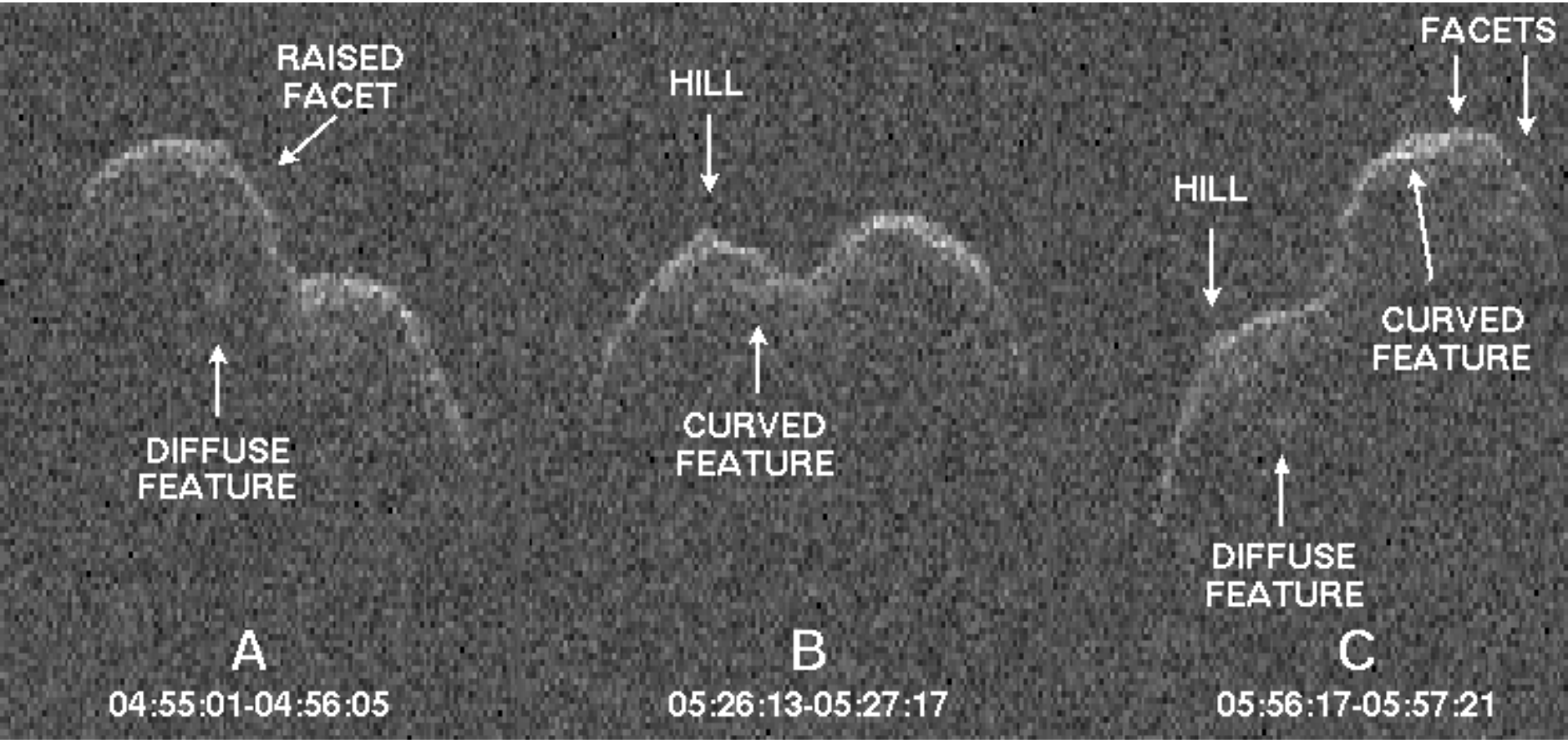

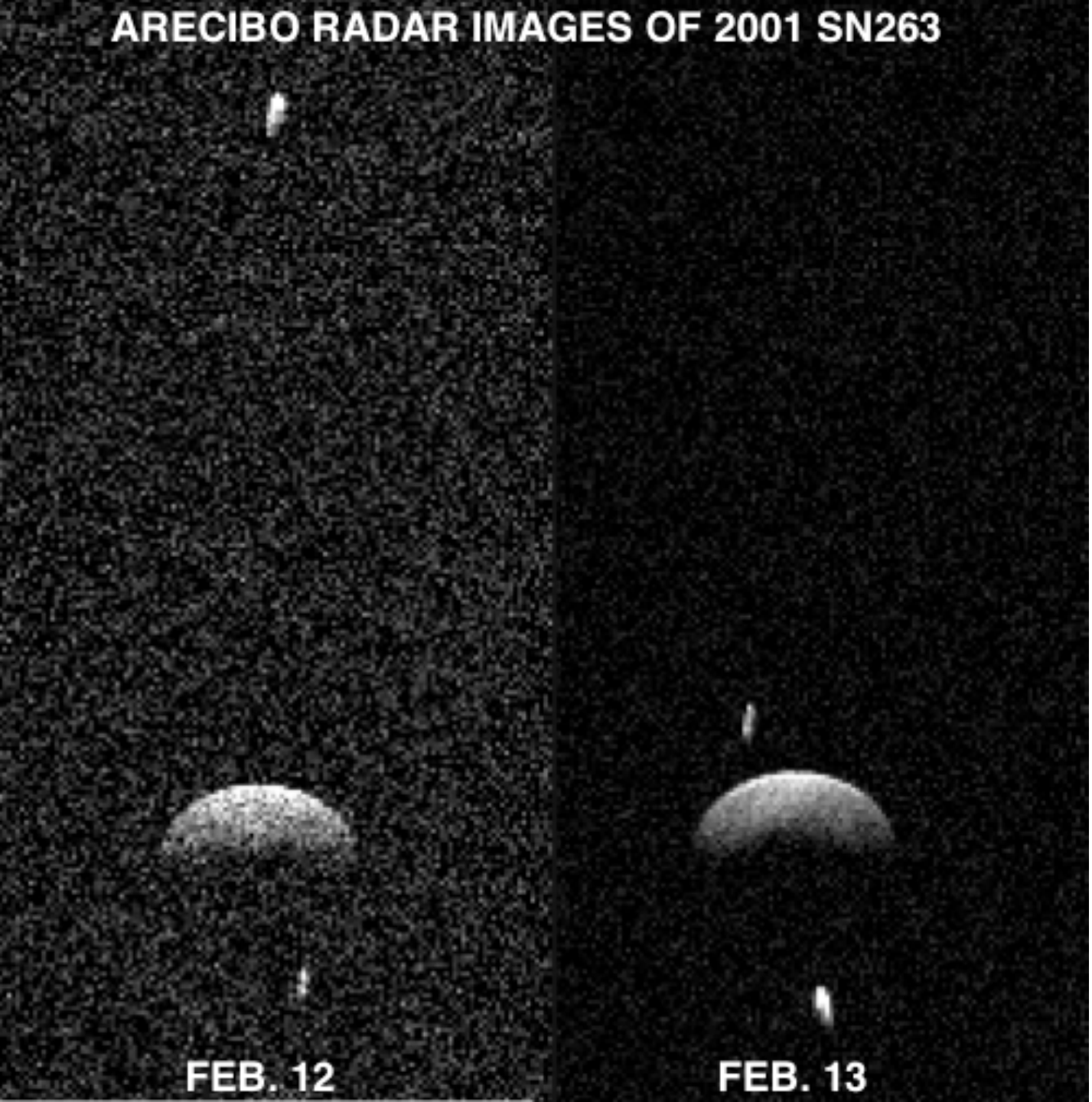

Triple Asteroid!

Mars radar images (Goldstone→VLA), 3.5 cm

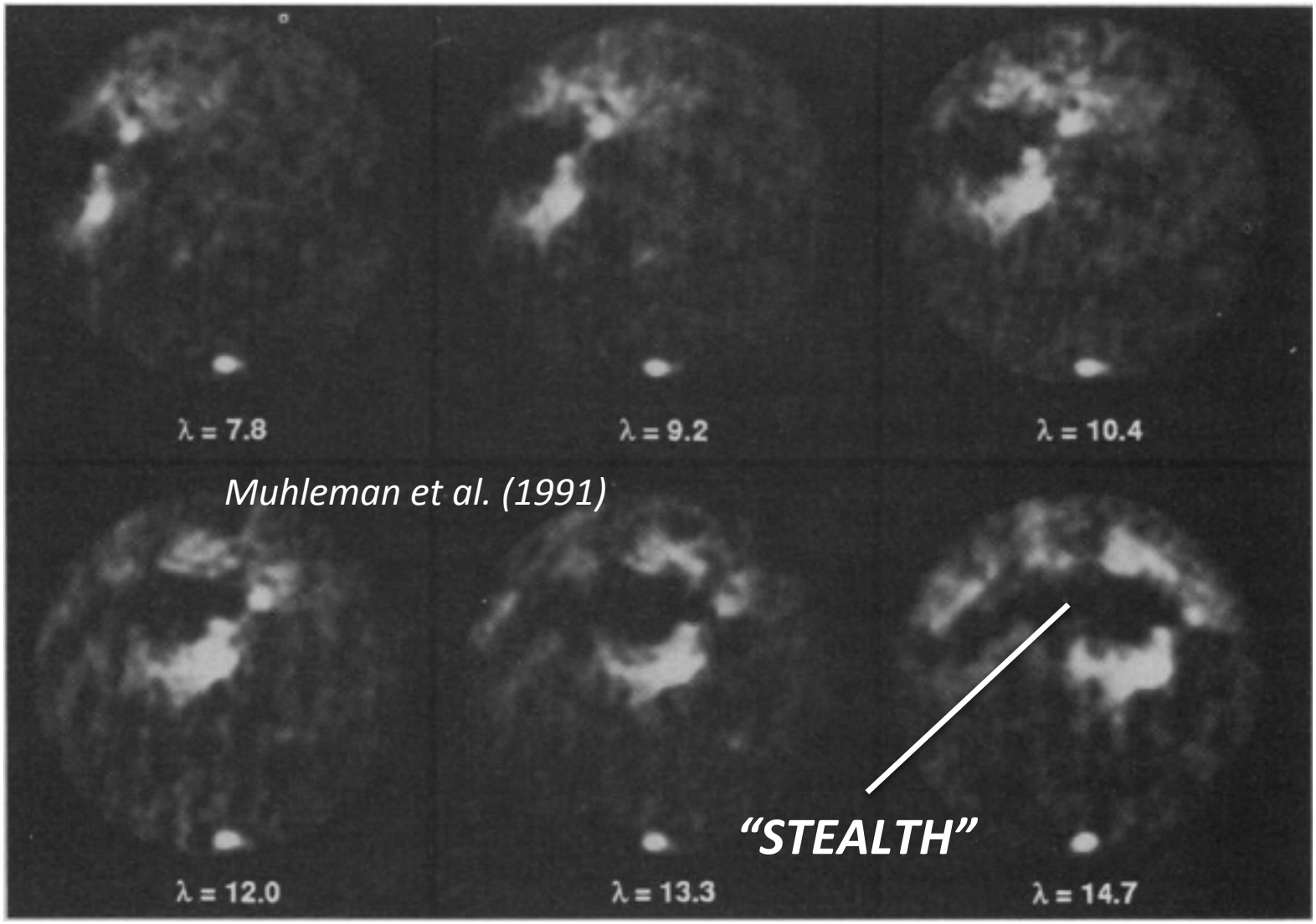

λ values are (erroneous) ***longitudes*** (should each be multiplied by 10)

Radar “stealth”: very low density, meters thick

Table 1. Major depolarized features.

Name*	Brightness† (Jy per beam)	Longitude (degrees)	Latitude (degrees)	Extent (km)‡ (north-south by east-west)
RSPIC	1.83 ± 0.04	53.2	−87.4	80 by 90
South Tharsis	1.31 ± 0.05	121.9	−21.0	85 by 240
Pavonis Mons	0.88 ± 0.02	107.4	0.6	85 by 100
Arsia Mons	0.77 ± 0.02	119.5	−9.1	80 by 100
Olympus Mons 1	0.70 ± 0.02	124.3	16.5	300 by 600
Olympus Mons 2	0.47 ± 0.02	156.5	14.9	185 by 260
Ascraeus Mons	0.64 ± 0.02	102.8	11.0	100 by 120
South Feature	0.36 ± 0.05	93.4	−40.9	70 by 140
Stealth	0.0 ± 0.02	125 to 168	0	500 by 2300
Average surface§	$\sim(0.15 \pm 0.02)\cos\theta_I$			

*The name is either taken from a nearby feature or invented here. †The brightness is the average of the brightest pixel from each snapshot and the rms value about this mean. The longitude and latitude value is the mean position of the brightest pixel averaged over the snapshots. ‡The extent is the rms wander of the surface position of the brightest pixel from the snapshots. It tends to be smaller than the region of half-brightness relative to the peak. For example, RSPIC is roughly 300 km in diameter but the brightest point is smaller. §θ_I is the angle of incidence of the radar beam.

Table 3. Depth of a Lossy dielectric sheet over a dielectric half-space that makes the conductor effectively invisible.

Density* (g cm^{-3})	Dielectric constant†	Reflectivity infinite layer (%)	Minimum depth (m)
0.1	$1.077 - i0.00086$	0.03	3.2
(0.1)	$(1.077 - i0.00043)$	(0.03)	(5.8)
0.2	$1.16 - i0.0019$	0.14	1.3
0.4	$1.33 - i0.0043$	0.51	0.65
(0.4)	$(1.33 - i0.00215)$	(0.51)	(1.25)
0.6	$1.53 - i0.0073$	1.12	0.45
0.8	$1.75 - i0.0112$	1.93	0.25
1.0	$2.00 - i0.0160$	2.95	<0.2

*The listings in parentheses have one-half the imaginary part of the dielectric constant above it, corresponding to less mafic materials, that is, less elemental iron. †Values for basaltic powders, packed with bulk densities given in column 1.

Muhleman et al. (1991)

Radar “stealth” zone, west of Tharsis volcanoes

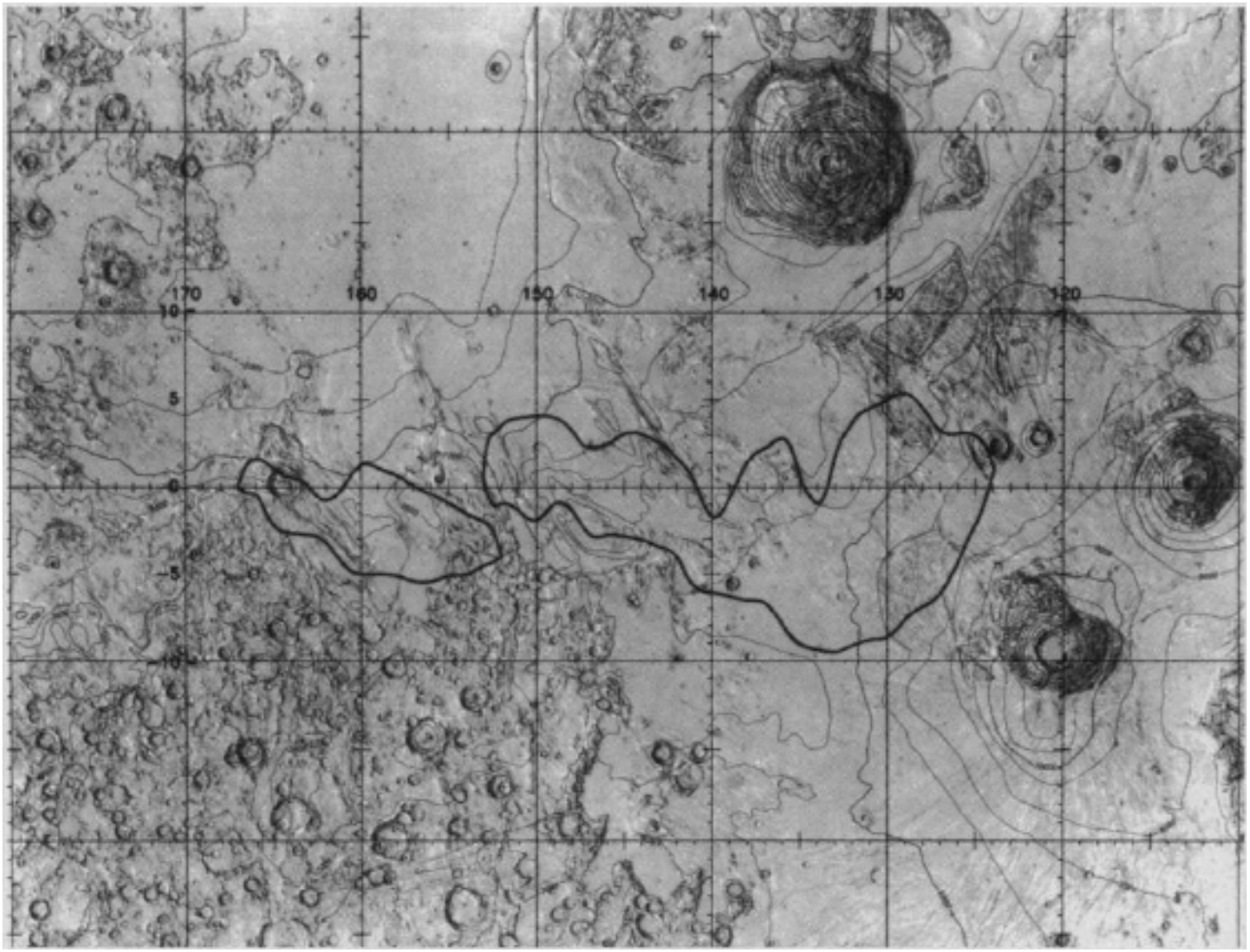

Muhleman et al. (1991)

“Stealth” also visible in passive microwave data

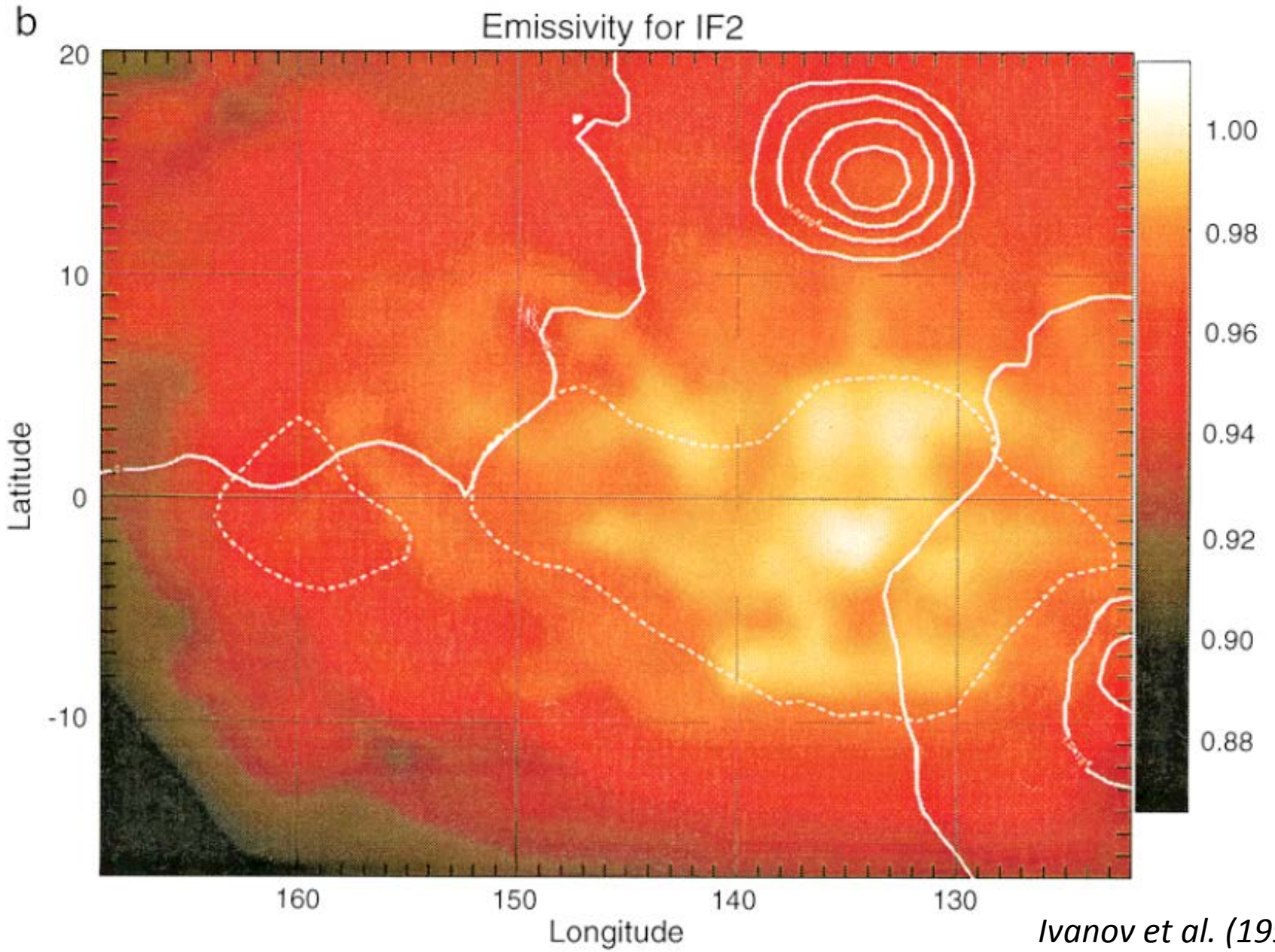

Ivanov et al. (1998)

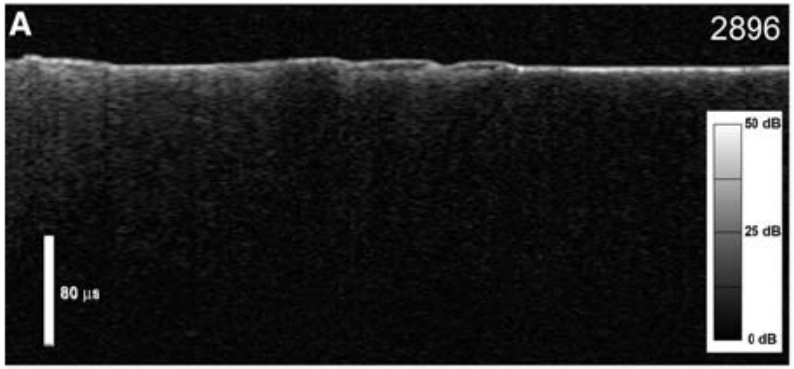

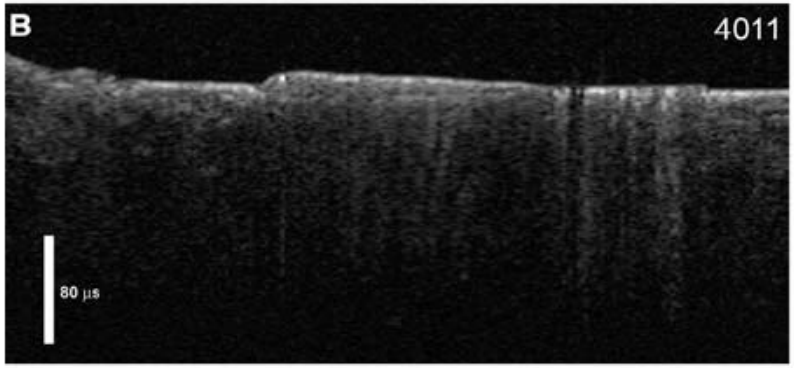

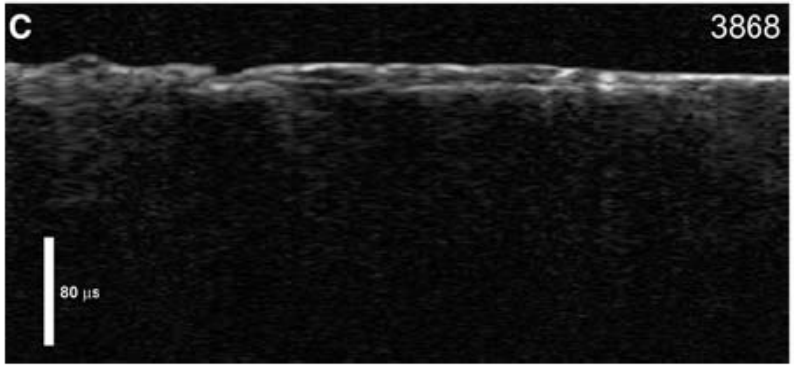

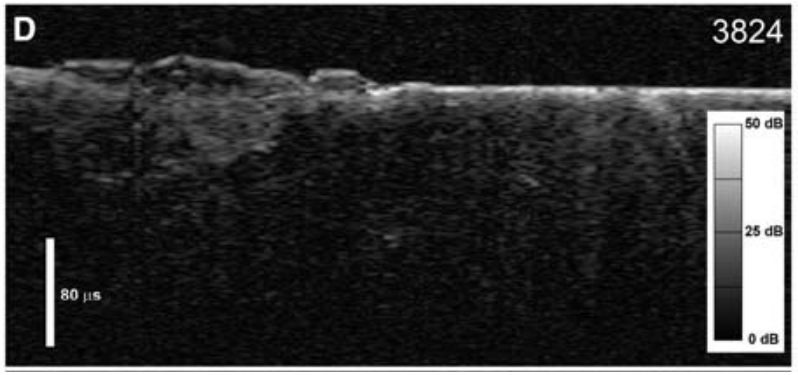

Radar Sounding of the Medusae Fossae Formation Mars: Equatorial Ice or Dry, Low-Density Deposits?

Thomas R. Watters,[1]* Bruce Campbell,[1] Lynn Carter,[1] Carl J. Leuschen,[2] Jeffrey J. Plaut,[3] Giovanni Picardi,[4] Roberto Orosei,[4] Ali Safaeinili,[3] Stephen M. Clifford,[5] William M. Farrell,[6] Anton B. Ivanov,[3] Roger J. Phillips,[7] Ellen R. Stofan[8]

The equatorial Medusae Fossae Formation (MFF) is enigmatic and perhaps among the youngest geologic deposits on Mars. They are thought to be composed of volcanic ash, eolian sediments, or an ice-rich material analogous to polar layered deposits. The Mars Advanced Radar for Subsurface and Ionospheric Sounding (MARSIS) instrument aboard the Mars Express Spacecraft has detected nadir echoes offset in time-delay from the surface return in orbits over MFF material. These echoes are interpreted to be from the subsurface interface between the MFF material and the underlying terrain. The delay time between the MFF surface and subsurface echoes is consistent with massive deposits emplaced on generally planar lowlands materials with a real dielectric constant of ~2.9 ± 0.4. The real dielectric constant and the estimated dielectric losses are consistent with a substantial component of water ice. However, an anomalously low-density, ice-poor material cannot be ruled out. If ice-rich, the MFF must have a higher percentage of dust and sand than polar layered deposits. The volume of water in an ice-rich MFF deposit would be comparable to that of the south polar layered deposits.

Units of the Medusae Fossae Formation (MFF) occur discontinuously at equatorial latitudes along the boundary of the hemispheric dichotomy from Amazonis to Elysium Planitiae (~130°E to 240°E) (*1*, *2*). The MFF may be among the youngest surficial deposits on Mars, unconformably overlying ancient Noachian heavily cratered highlands and young Amazonian lowlands (*1*–*8*). However, pedestal craters on the outer edge of the MFF

LIDAR: Mars Orbiter Laser Altimeter

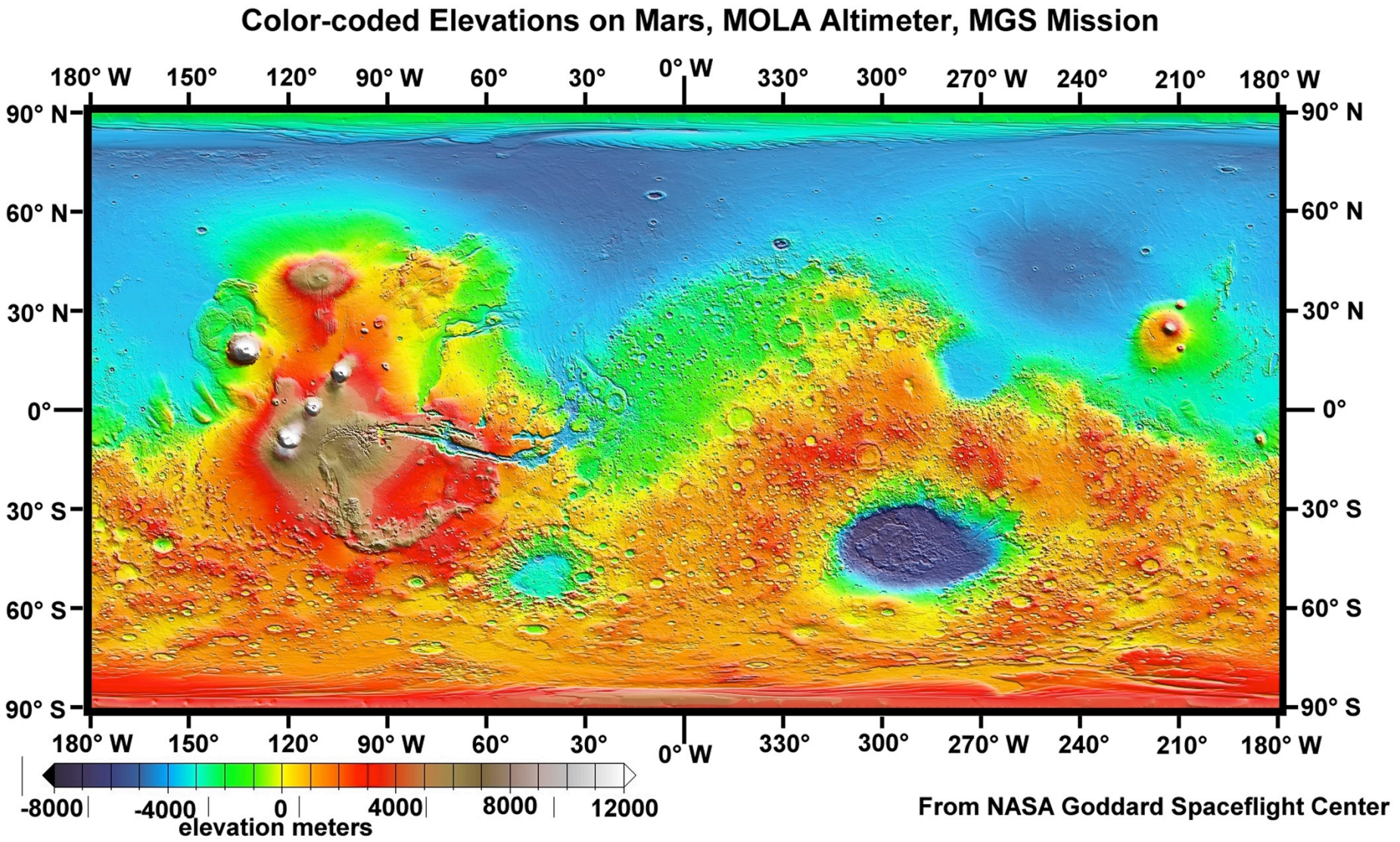

How MOLA makes its Range Measurement

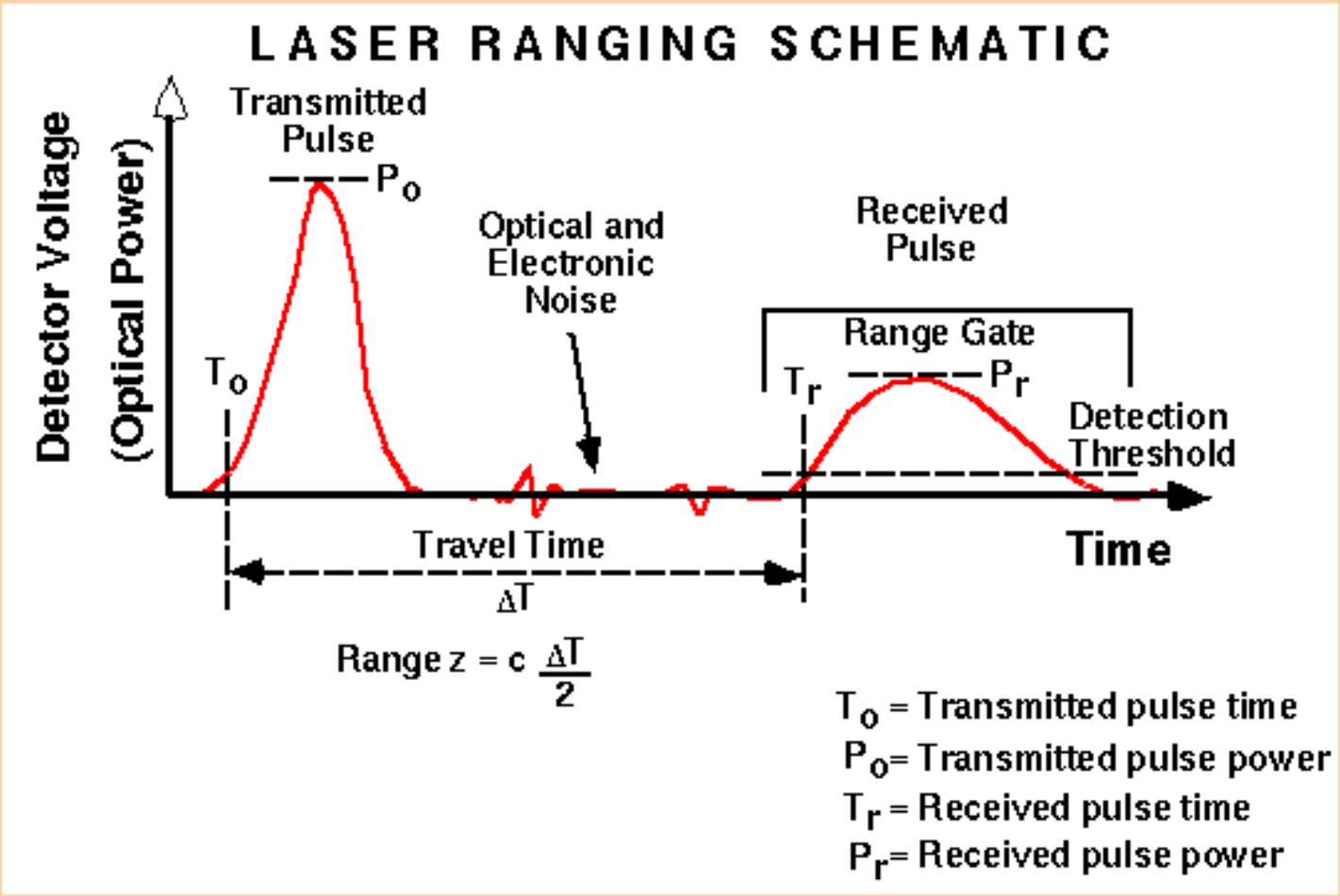

Table 1. MOLA Instrument Specifications

Parameter	Specification
Mass	23.8 kg
Power consumption[a]	34.2 W
Transmitter	
Laser type	diode pumped, Q-switched, Cr:Nd:YAG
Wavelength	1.064 μm
Pulse rate	10 Hz
Energy[b]	48 mJ pulse^{-1}
Laser divergence	420 μrad
Pulse length	8 ns
Receiver	
Mirror	50-cm parabolic
Detector	silicon avalanche photodiode
Field of view	850 μrad
Electronics	
Microprocessor	80C86
TIU frequency	99.996 MHz
Filter channel widths	20, 60, 180, 540 ns
Data rate	618 bits s^{-1} continuous
Resolution	
Maximum ranging distance[c]	787 km
Range resolution	37.5 cm
Vertical accuracy[d]	1 m
Surface spot size[e]	168 m
Along-track shot spacing	300 m
Across-track shot spacing[f]	4 km

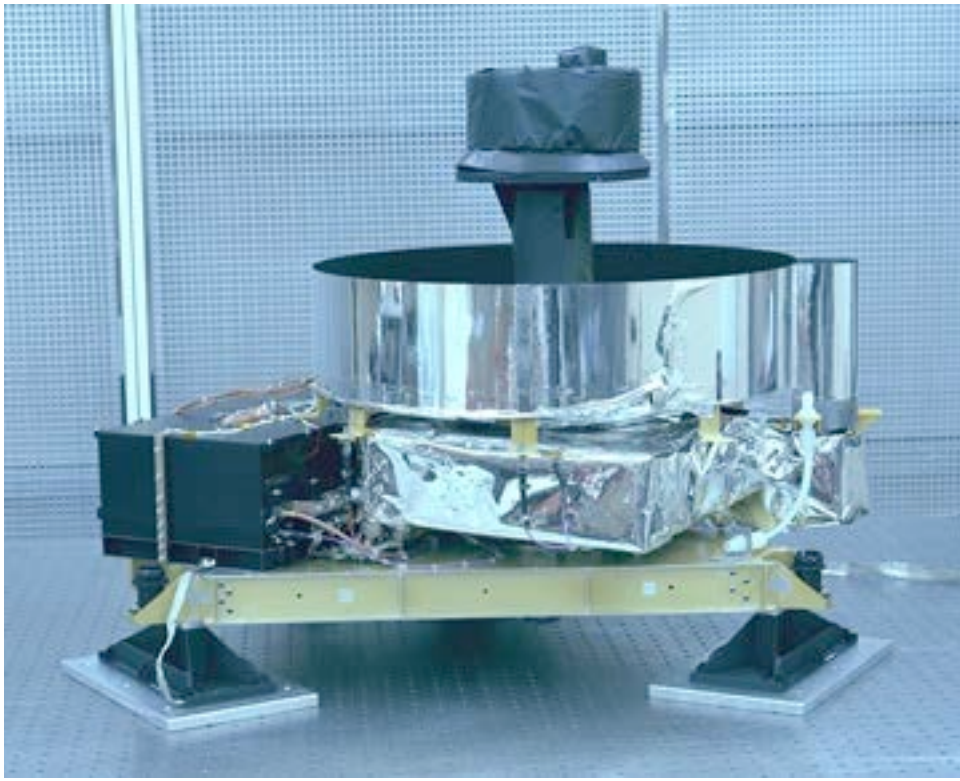

[a] Includes replacement heat for temperature control.
[b] At arrival at Mars; degrades with time.
[c] Hardware limited.
[d] Includes radial orbit error.
[e] In 400-km-elevation mapping orbit.
[f] Average at equator; varies with cos(latitude).

LOLA

Lunar Orbiter Laser Altimeter

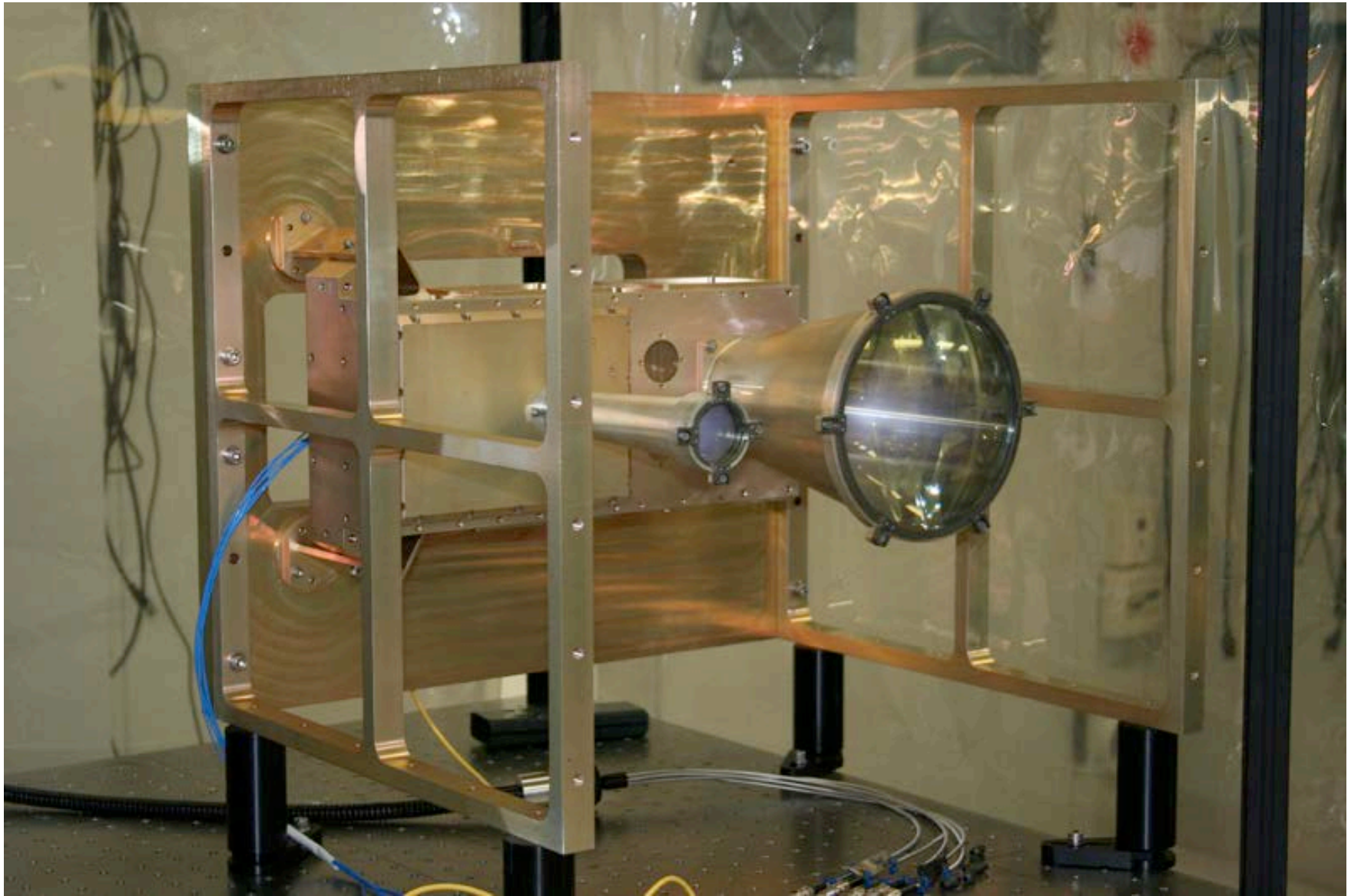

LOLA

Lunar Orbiter Laser Altimeter

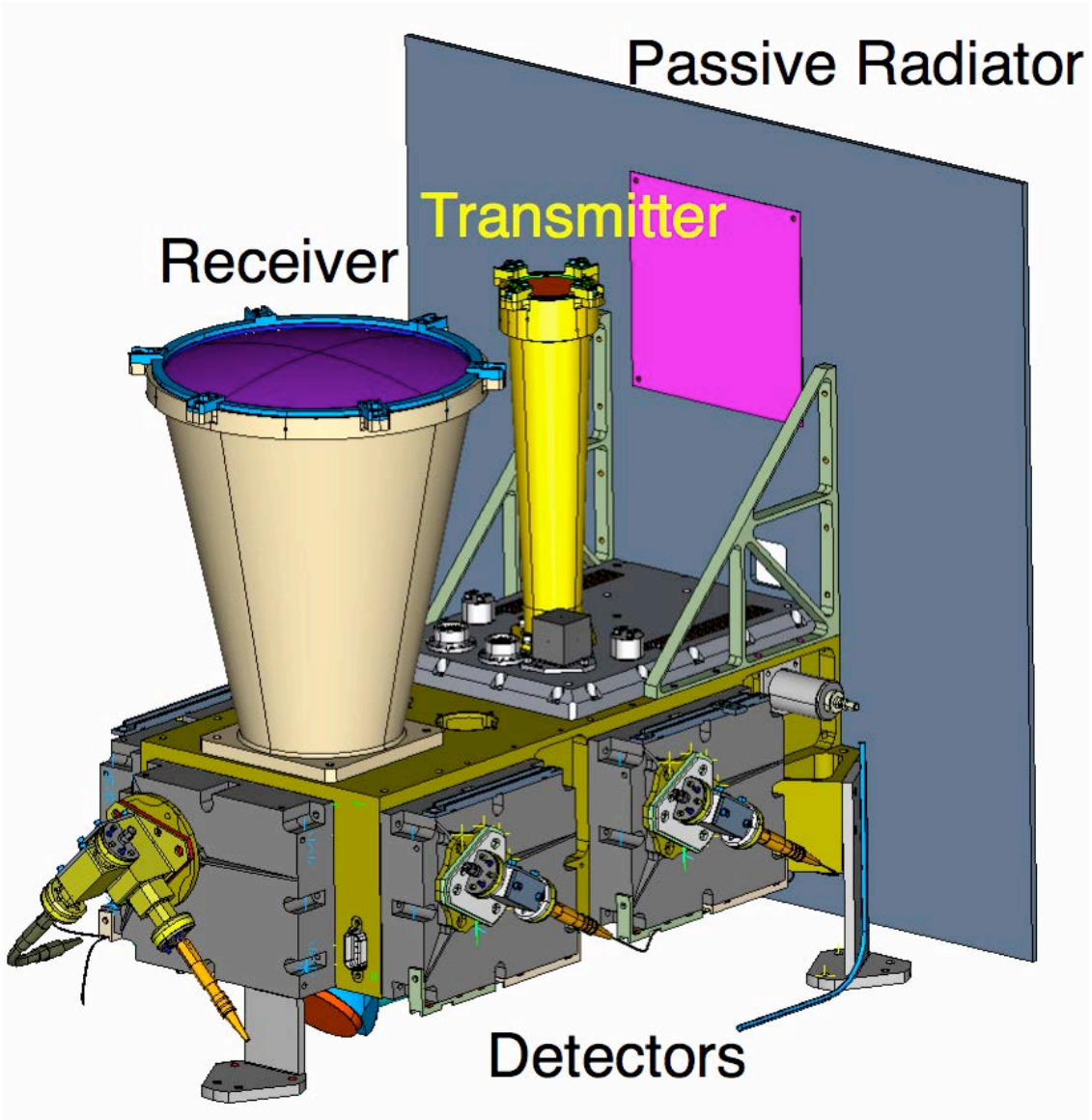

LOLA

Lunar Orbiter Laser Altimeter

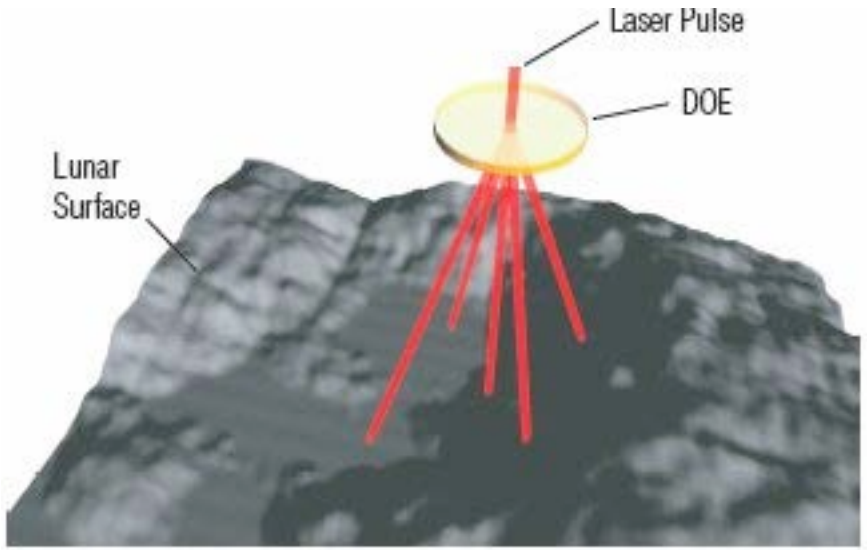

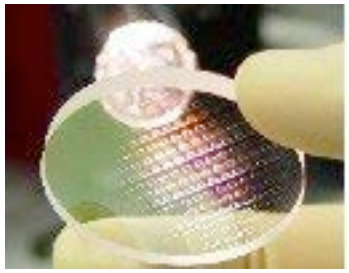

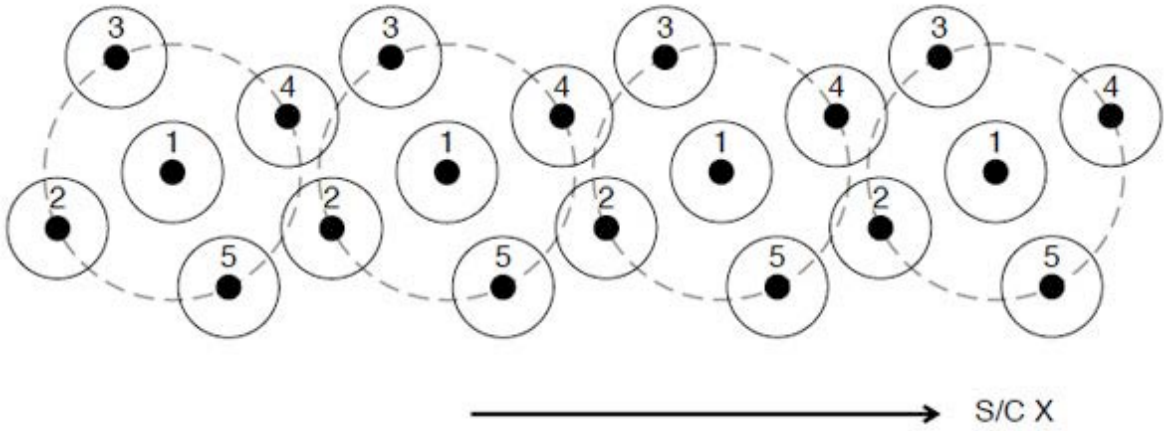

LOLA results

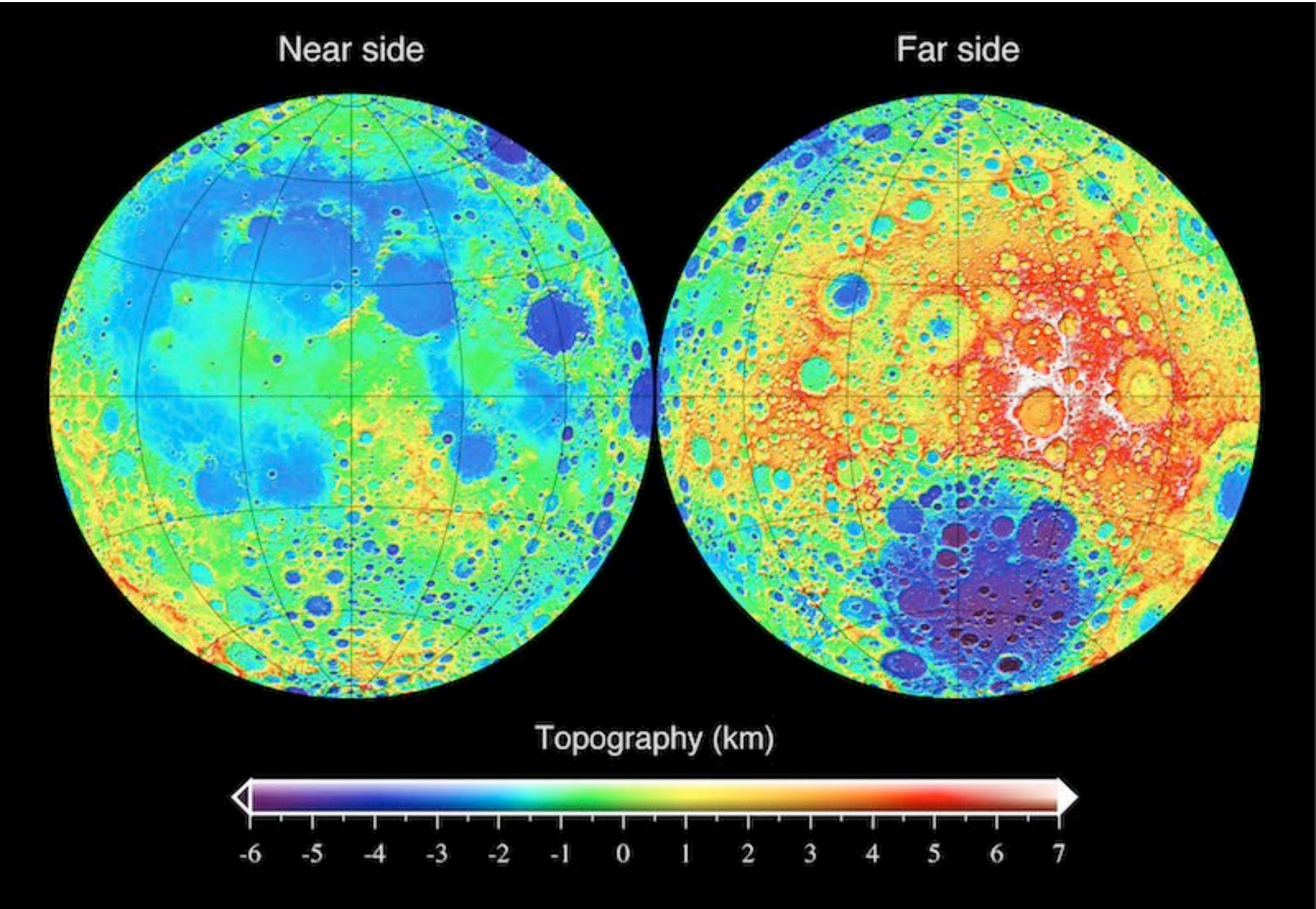

Planetary lidar: siblings of MOLA, LOLA

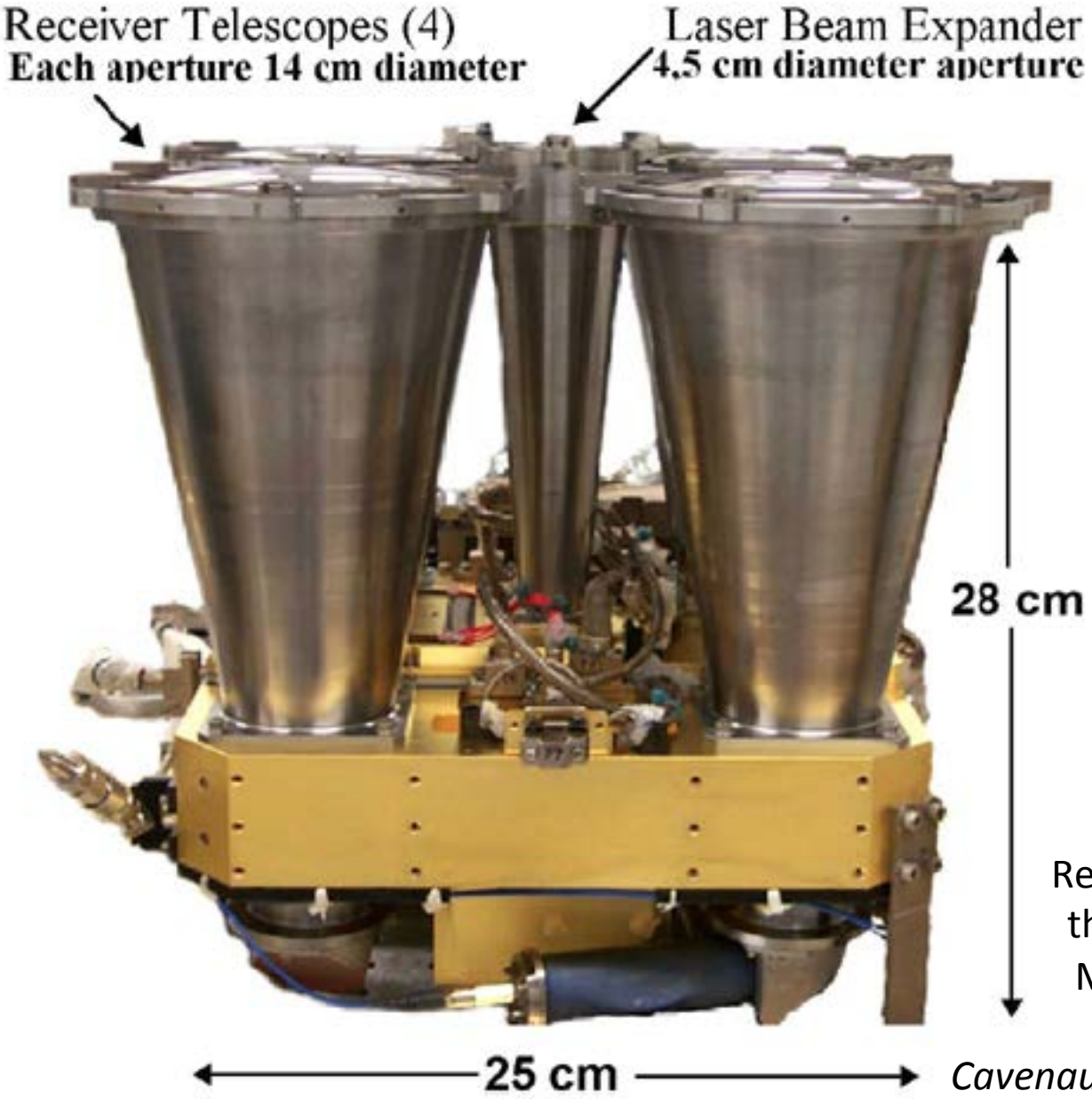

Refractive optics chosen instead of the usual reflective, to withstand Mercury's thermal environment

Cavenaugh et al. (2007)

MESSENGER's Mercury Laser Altimeter (MLA)

Measures topography, 1064 nm reflectivity ***within <800 km of surface***

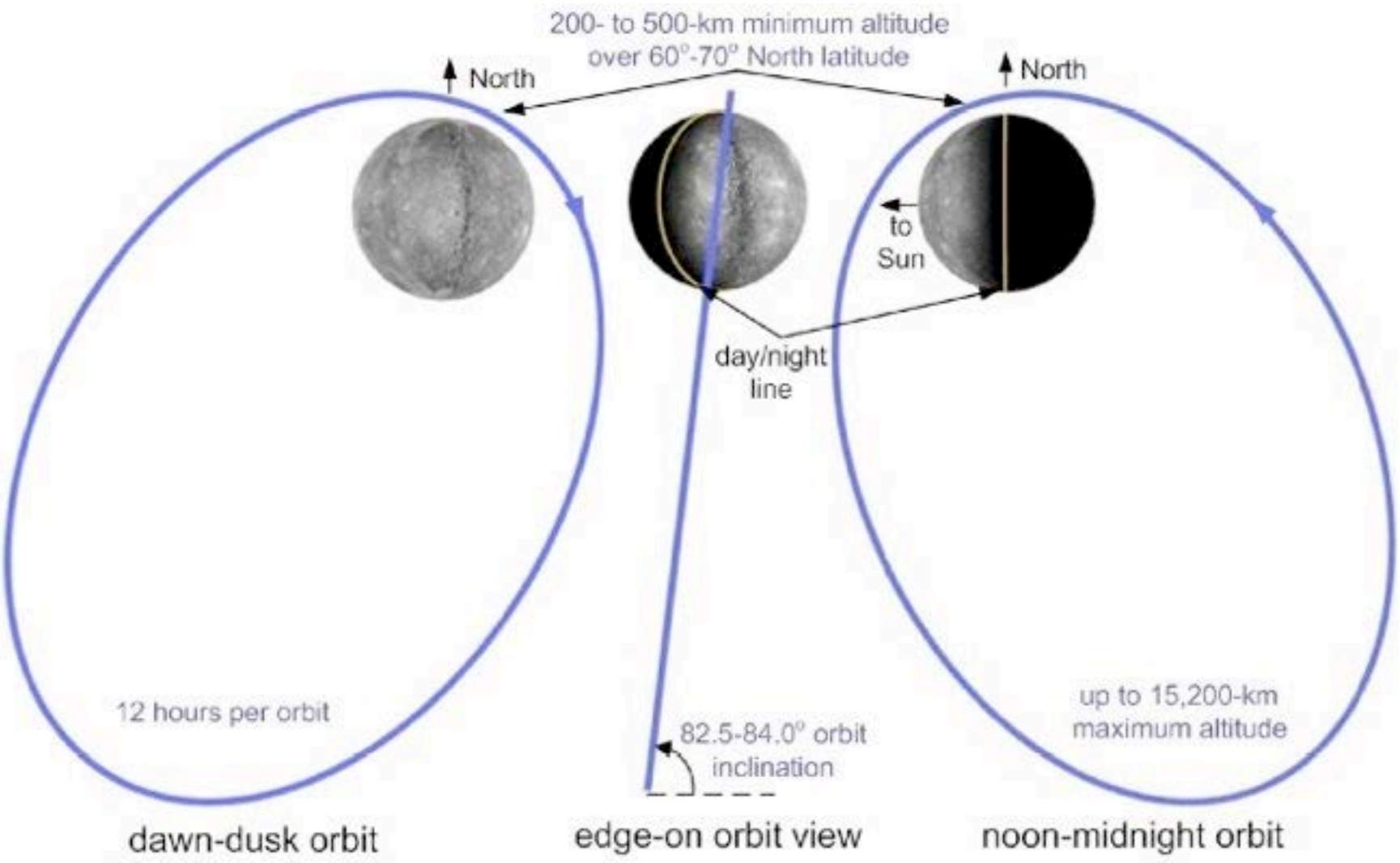

MESSENGER's Mercury Laser Altimeter (MLA)

Topography
from ~55 to 90° N

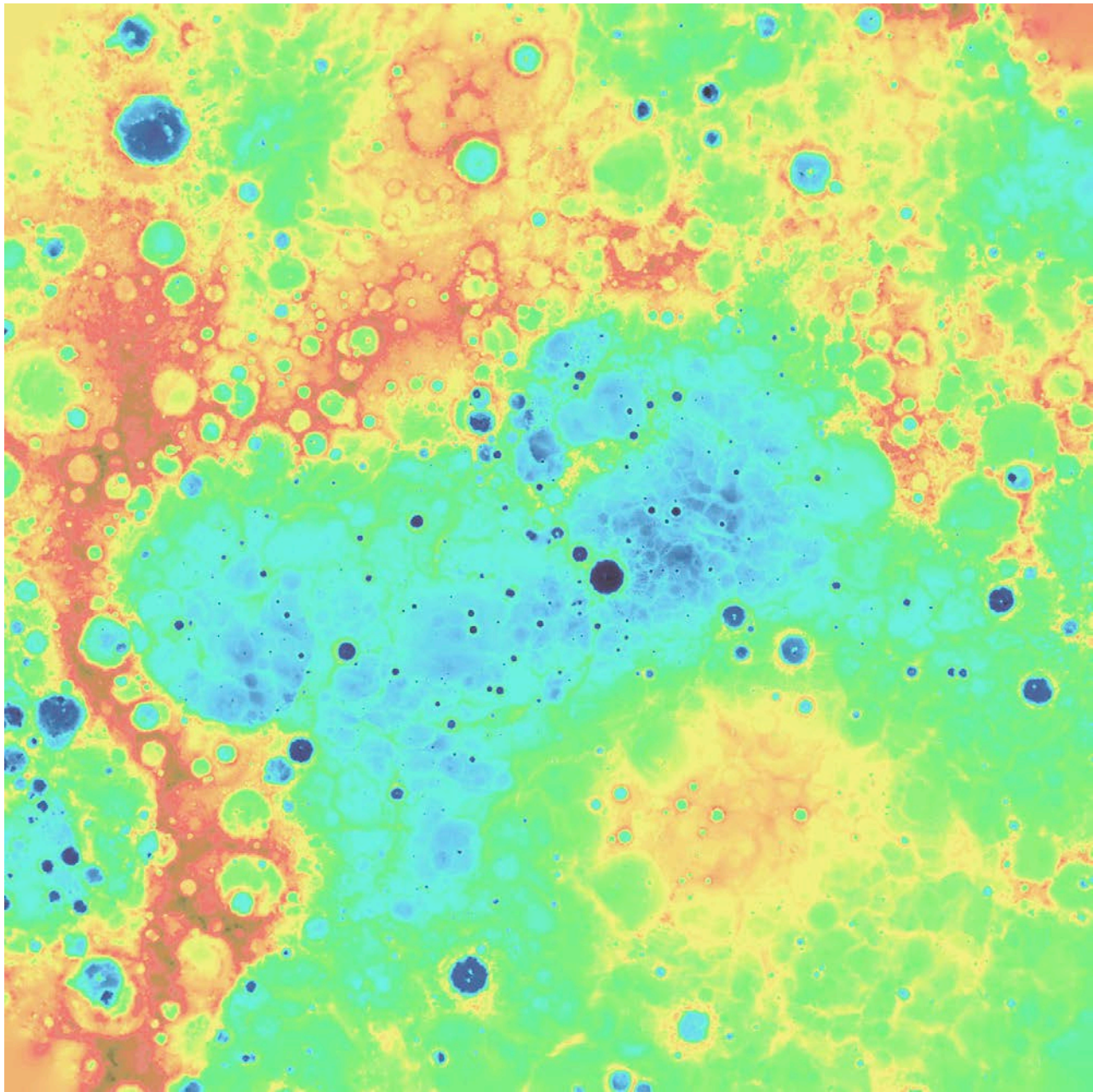

Planetary lidar: siblings of MOLA, LOLA

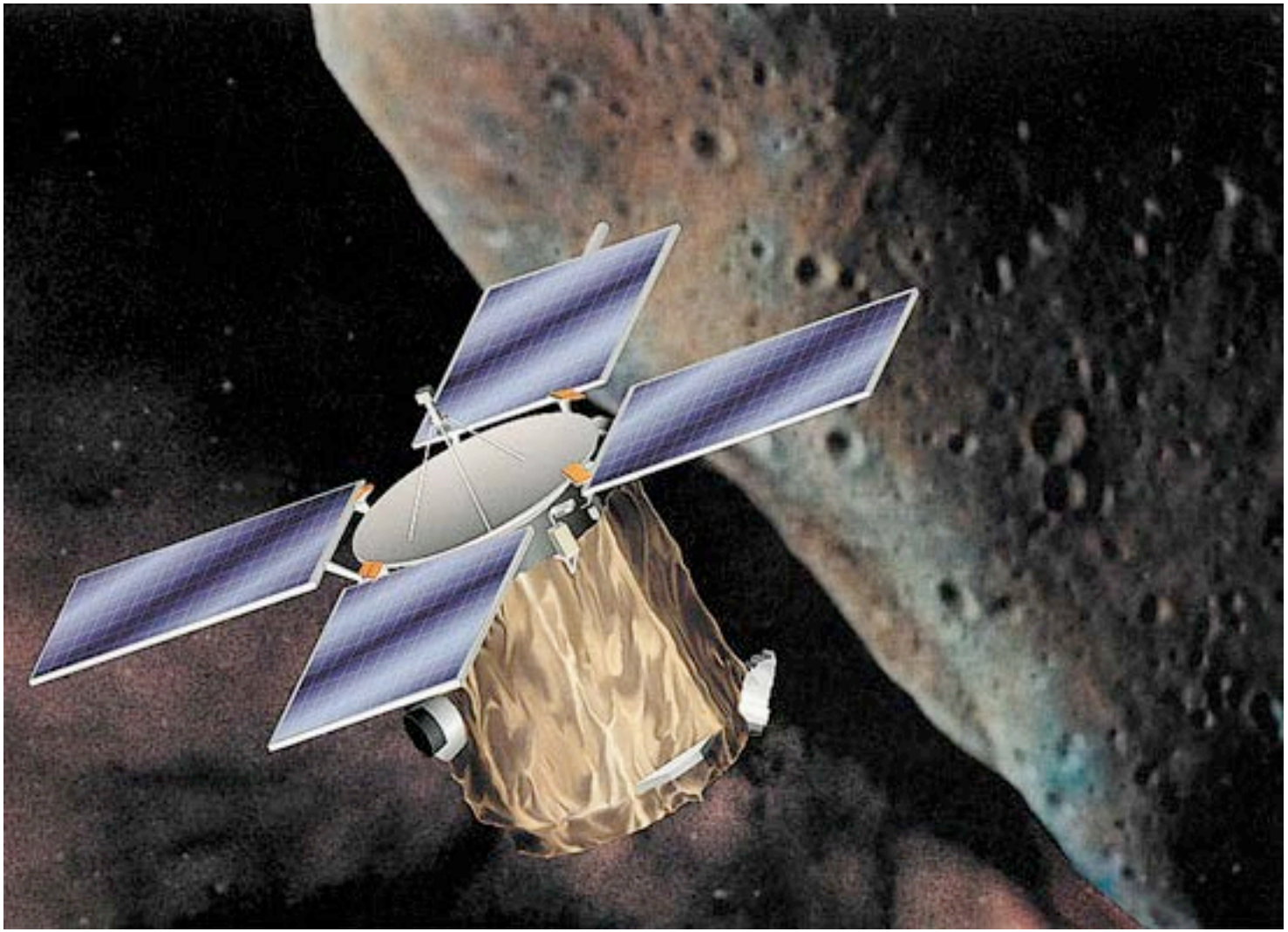

NEAR Laser Rangefinder (NLR) on the Near Earth Asteroid Rendezvous (NEAR) mission

NEAR Laser Rangefinder (NLR) on the Near Earth Asteroid Rendezvous (NEAR) mission

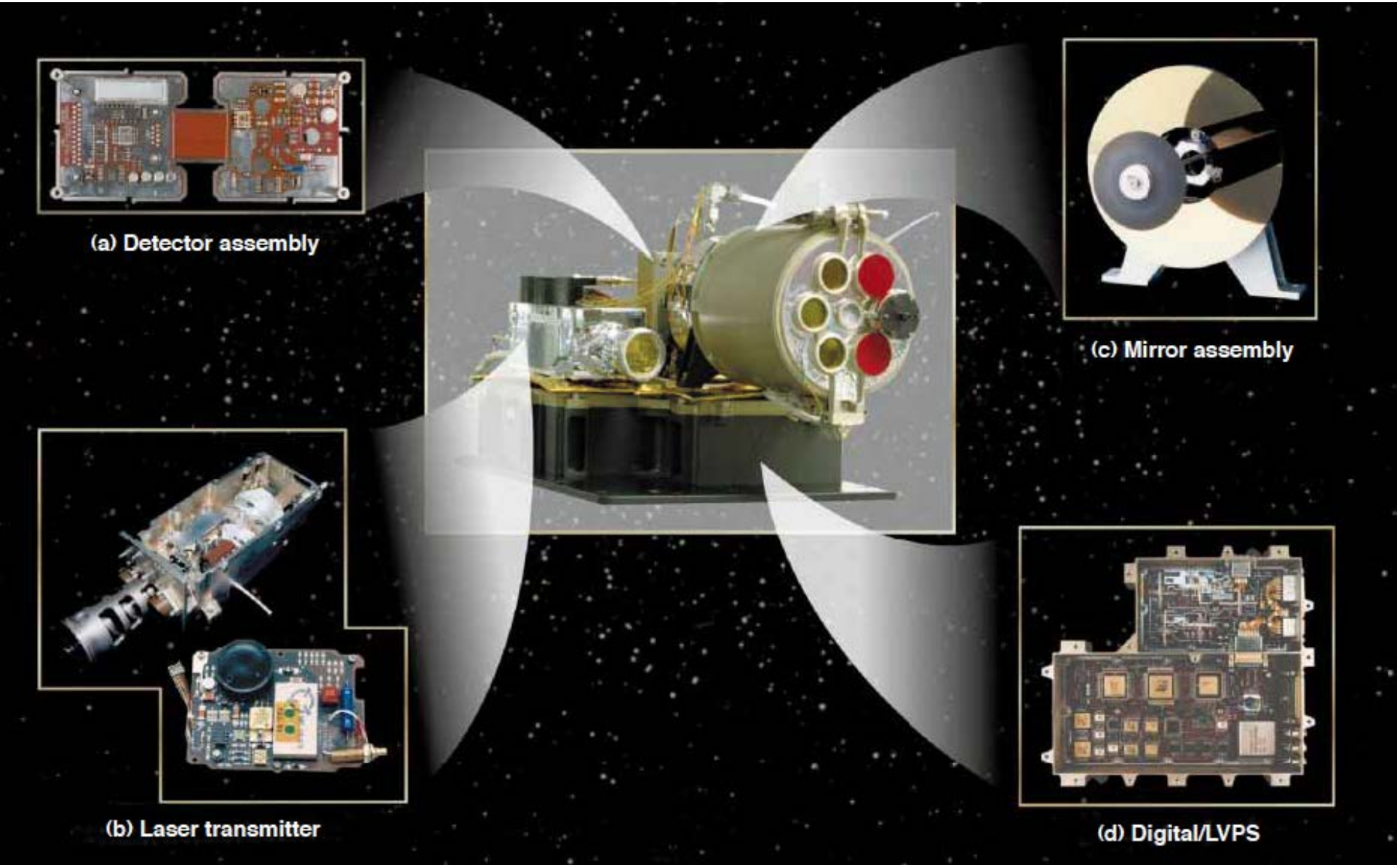

NEAR Laser Rangefinder (NLR) on the Near Earth Asteroid Rendezvous (NEAR) mission

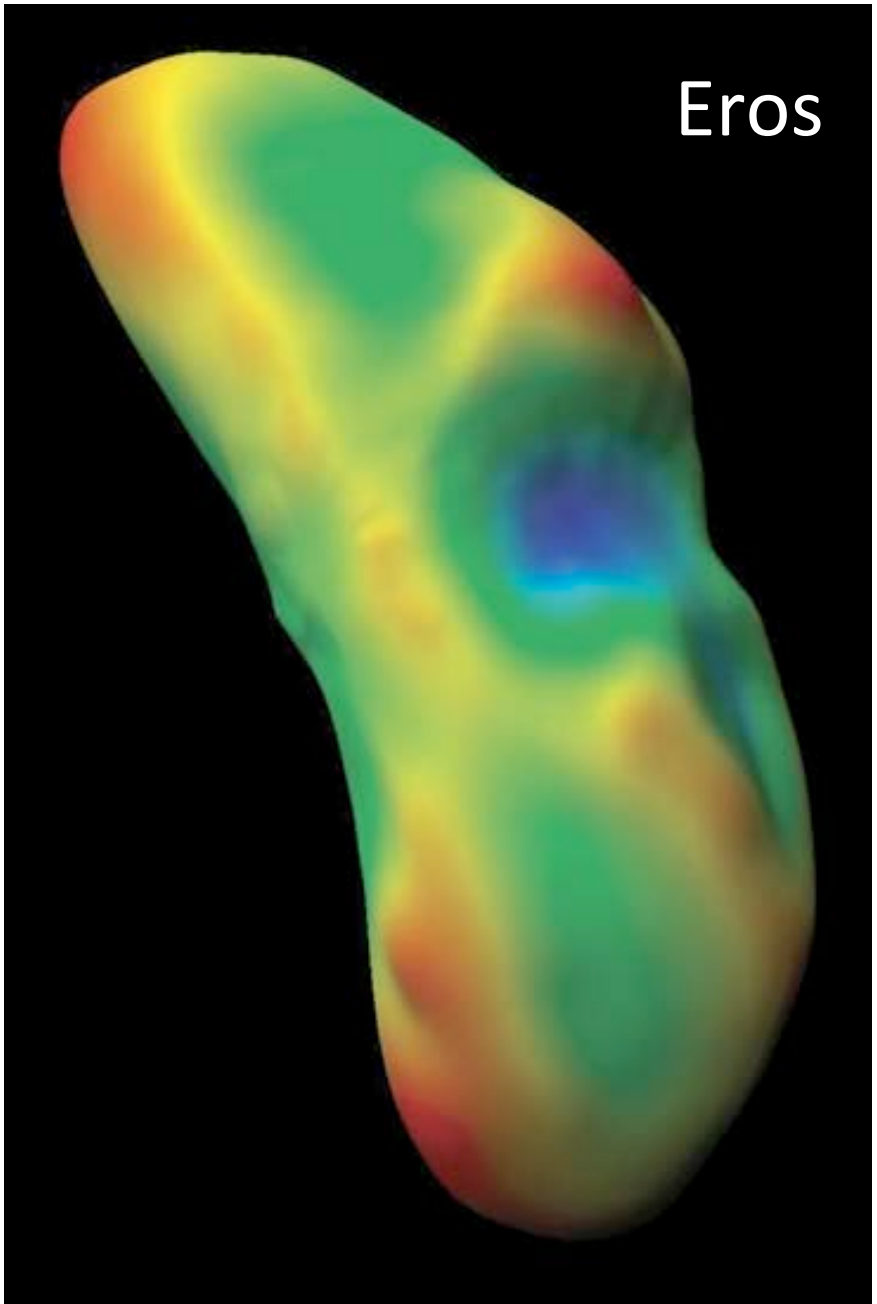

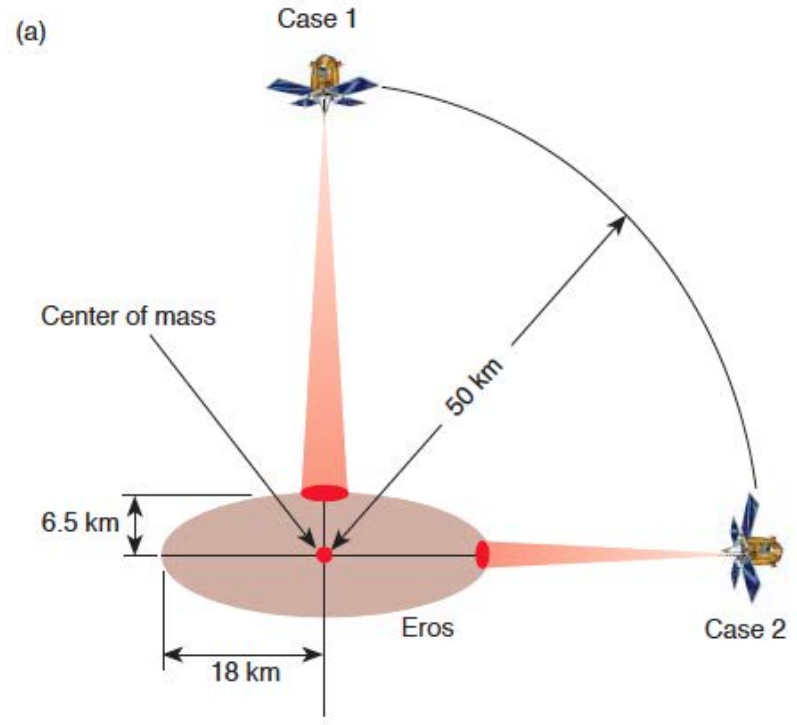

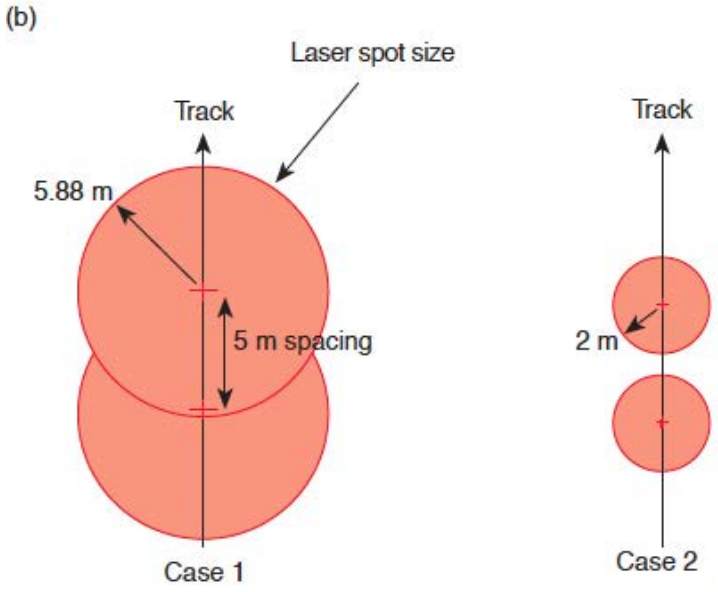

NEAR Laser Rangefinder (NLR) on the Near Earth Asteroid Rendezvous (NEAR) mission

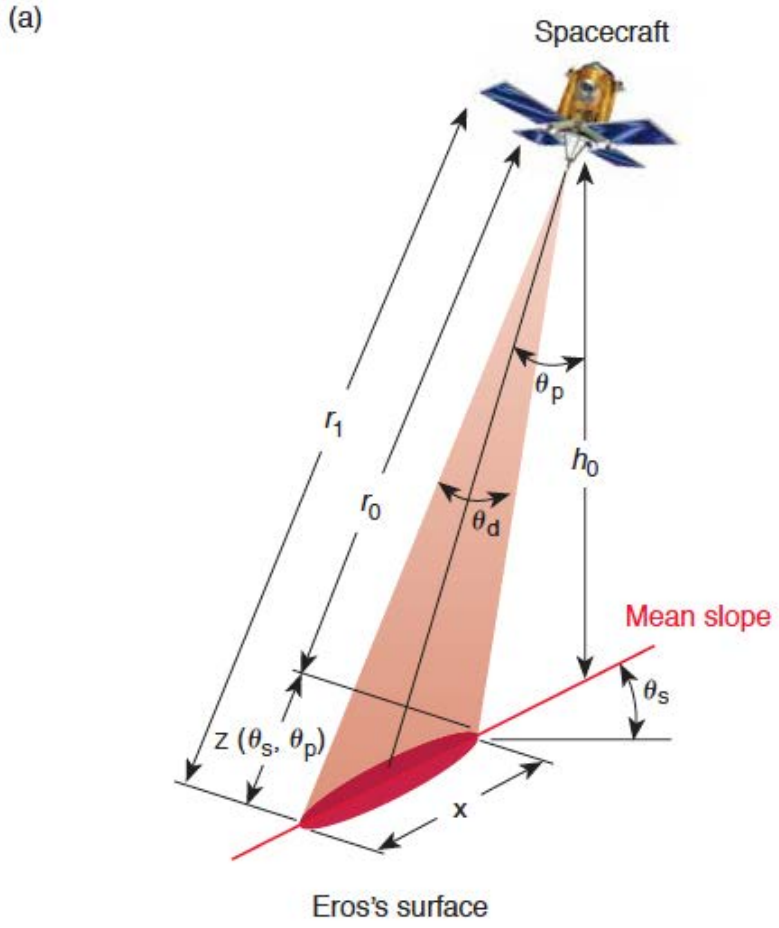

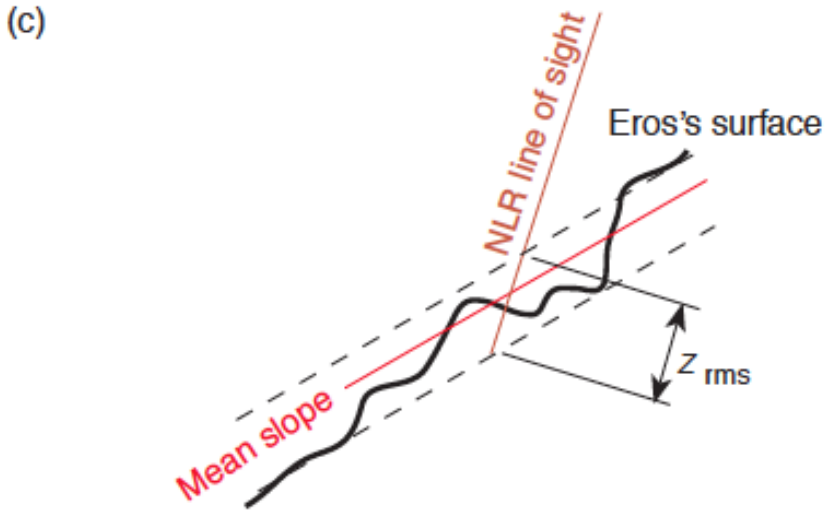

Figure 13. Diagram explaining pulse dilation occurring as the pulse interacts with the asteroid's surface. Various parameters describing the spacecraft's look angle are presented in (a), which give rise to pulse dilated returns, defined by (b). As the pulse is transmitted from the NLR, the pulse duration is relatively sharp and small, ≈15 ns. As the pulse incurs extended aspects of the surface, significant backscatter dilation starts to occur. This "distributed" return manifests itself by stretching the pulse over the finite extent of the range gate used. (c) The details associated with rough surface pulse stretching are shown. R = measured range; z_{rms} = surface roughness.